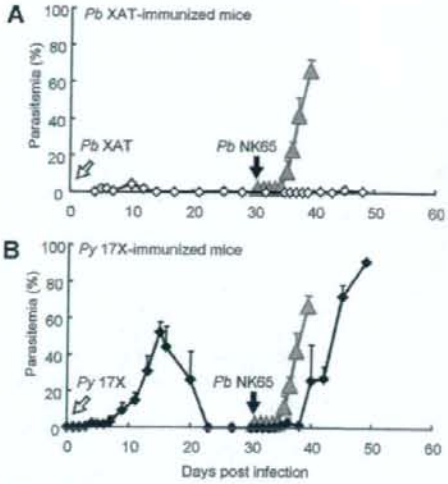

FIGURE 1. Immunization with *Pb* XAT but not *Py* 17X induces protective immunity to *Pbi* NK65. C57BL/6 mice were infected with 1×10^4 pRBCs of *Pb* XAT (*A*) or *Py* 17X (*B*) (day 0, open arrows). On day 30 after primary infection (filled arrows), both groups of mice were challenged with 1×10^4 pRBCs of *Pb* NK65. *A*, Course of parasitemia in immunized mice with *Pb* XAT (◇). *B*, Course of parasitemia in immunized mice with *Py* 17X (◆). Course of parasitemia of unimmunized mice infected with *Pb* NK65 is inserted to figures (shaded triangles). Results are expressed as mean percentage parasitemia ± SD of three mice. Experiments were performed three times with similar results.

The pathogenesis during Pb *NK65 infection is reduced by simultaneous infection with nonlethal malaria parasites*

To investigate whether the existence of nonlethal malaria parasite affects the outcome of *Pb* NK65 infection, B6 mice were infected with *Pb* NK65 and nonlethal parasites simultaneously. When mice were coinfected with *Pb* NK65 and *Pb* XAT (*Pb* NK65/*Pb* XAT), they showed lower levels of parasitemia than did *Pb* NK65 singly infected mice during early infection (Fig. 2*A*) and survived significantly longer than did *Pb* NK65 singly infected mice (Fig. 2*B*) ($p = 0.0013$). Moreover, the body weight loss of the coinfected mice was prevented early in infection (Fig. 2*C*) ($p < 0.0005$ compared with *Pb* NK65-infected mice on days 9–10). Next, we examined the influence of coinfection with nonlethal *Py* 17X on the outcome of *Pb* NK65 infection. Although *Py* 17X immunization did not affect the outcome of *Pb* NK65 infection greatly (Fig. 1*B*), simultaneous infection with *Py* 17X (*Pb* NK65/*Py* 17X) suppressed severe parasitemia, mortality ($p = 0.0005$), and the body weight loss ($p < 0.0005$ on days 6–10) observed in *Pb* NK65 singly infected mice (Fig. 2, *D–F*).

Coinfection with nonlethal malaria parasites induces reticulocytemia

To examine whether the existence of nonlethal malaria parasites affects the severe anemia caused by *Pb* NK65 infection, we determined the hematocrit in mice during *Pb* NK65 single infection and coinfection with *Pb* XAT or *Py* 17X. Coinfection with *Pb* XAT caused acute anemia as severe as did *Pb* NK65 single infection on day 9 postinfection, and the levels of hematocrit were also low on day 15 (Fig. 3*A*). Mice infected with *Pb* XAT did not cause acute severe anemia. In contrast, mice coinfected with *Pb* NK65/*Py* 17X did not cause as severe anemia as for *Pb* NK65-infected mice on day 9, and their reducing pattern of hematocrit was similar to that in *Py* 17X singly infected mice (Fig. 3*C*).

Next, we determined the reticulocytemia in infected mice. *Pb* NK65 singly infected mice did not show any reticulocytemia during infection (Fig. 3*B*). Mice coinfected with *Pb* NK65/*Pb* XAT showed the same levels of reticulocytemia as did *Pb* XAT singly infected mice on day 9 postinfection. However, coinfected mice showed much higher reticulocytemia than that in *Pb* XAT singly infected mice from day 11 postinfection (Fig. 3*B*). As shown in Fig. 3*D*, reticulocytemia in mice coinfected with *Pb* NK65/*Py* 17X increased moderately, and their kinetics were similar to those in *Py* 17X singly infection. These results indicate that the severe anemia caused by *Pb* NK65 infection is suppressed by coinfection with *Py* 17X but not with *Pb* XAT. It is suggested that high levels of reticulocytemia observed during *Pb* NK65/*Pb* XAT infection may

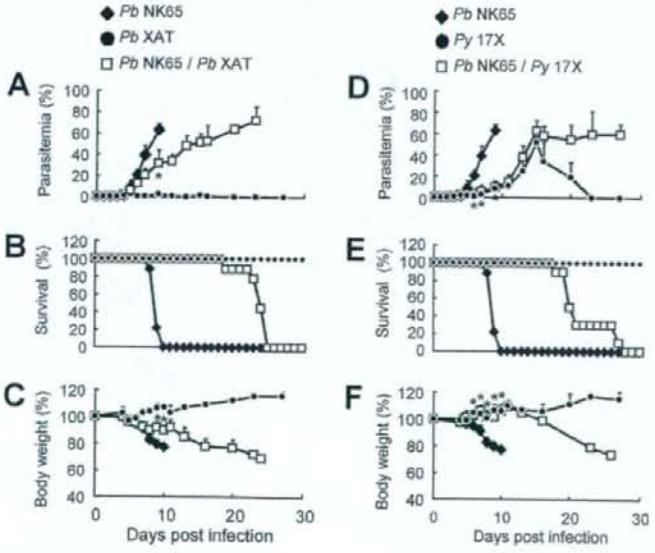

FIGURE 2. Coinfection of nonlethal *Pb* XAT or *Py* 17X suppresses the acute severe parasitemia and body weight loss caused by *Pb* NK65 infection in mice and prolonged their survival. C57BL/6 mice were inoculated with 1×10^4 pRBCs of *Pb* NK65, *Pb* XAT, or *Py* 17X. When mice were coinfected with two species/strains of parasites, a total of 2×10^4 pRBCs were inoculated (*Pb* NK65/*Pb* XAT or *Pb* NK65/*Py* 17X). Results of coinfection are shown for *Pb* NK65/*Pb* XAT (*A–C*) or *Pb* NK65/*Py* 17X (*D* and *E*). *A* and *D*, Course of parasitemia. Asterisks indicate statistically significant differences (*, $p < 0.001$ as compared with *Pb* NK65-infected mice). *B* and *E*, Survival rates. Differences between *Pb* NK65 singly infected mice and coinfected mice are statistically significant ($p < 0.001$). *C* and *F*, Body weights. Asterisks indicate statistically significant differences (*, $p < 0.001$ as compared with *Pb* NK65-infected mice). Results are expressed as means ± SD of five mice. Experiments were performed three times with similar results.

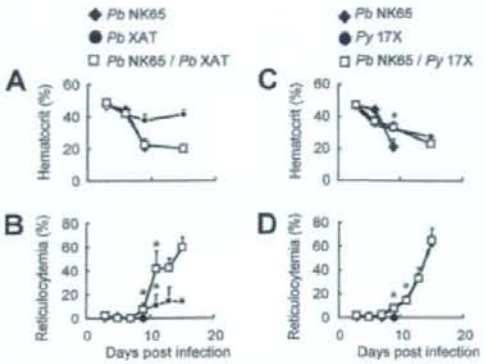

FIGURE 3. Coinfection with nonlethal malaria parasites induces reticulocytemia. Mice were infected with malarial parasites as described in the legend to Fig. 2. *A* and *C*, Blood (50 μl) was collected from infected mice on days 3, 6, 9, and 15 after infection and hematocrit values were determined. *B* and *D*, Reticulocytemia was determined on days 3, 5, 7, 9, 11, 13, and 15 after infection. The percentage of reticulocytemia was calculated as follows: [(number of reticulocytes)/(total number of RBCs counted)] × 100. Asterisks indicate a statistically significant difference (*, $p < 0.001$ as compared with *Pb* NK65-infected mice). Results are expressed as means ± SD of three mice. Experiments were performed three times with similar results.

be induced by severe anemia. The different outcome of the suppression of anemia and reticulocytemia between *Pb* NK65/*Pb* XAT- and *Pb* NK65/*Py* 17X-infected mice might be attributed to the difference in parasitemia during early infection.

Low levels of liver injury in mice coinfected with nonlethal malaria parasites

To investigate whether the existence of nonlethal malaria parasites affects the liver injury caused by *Pb* NK65 infection, we performed histological examination of livers from mice during *Pb* NK65 single infection and coinfection with *Pb* XAT or *Py* 17X. As shown in Fig. 4, focal necrosis of the liver cells (Fig. 4, *B* and *F*, arrowheads) and dense infiltration of inflammatory cells such as mononuclear cells around the portal tracts (Fig. 4*F*, arrows) were observed in *Pb* NK65-infected mice. Mice coinfected with *Pb* NK65/*Pb* XAT or *Pb* NK65/*Py* 17X also showed dense infiltration of inflammatory cells (Fig. 4, *G* and *H*, arrows), but focal necroses were not observed in the liver (Fig. 4, *C* and *D*).

We determined the levels of AST and ALT, which are parameters of liver injury, in the plasma. *Pb* NK65-infected mice, in which the focal necroses of liver cells were observed, showed the significantly high concentration of AST and ALT compared with uninfected control mice (Fig. 4, *I* and *J*). The levels of AST and ALT in coinfected mice were quite low and almost the same as those in *Pb* XAT or *Py* 17X singly infected mice.

Coinfection with nonlethal parasites accelerates $B220^{int}CD11c^{+}$ cell expansion in spleen and peripheral blood

To examine the expansion of the $CD11c^{+}$ cell populations during malaria, additional experiments were performed using peripheral blood and spleen obtained from infected mice by flow cytometry in each time point after infection. It was notable that the $B220^{int}CD11c^{+}$ cell population significantly increased in peripheral blood from *Pb* NK65/*Pb* XAT- or *Pb* NK65/*Py* 17X-coinfected mice on day 6 postinfection (Fig. 5*A*, *upper panels*). Their expansion was comparable to that observed in *Pb* XAT or *Py* 17X

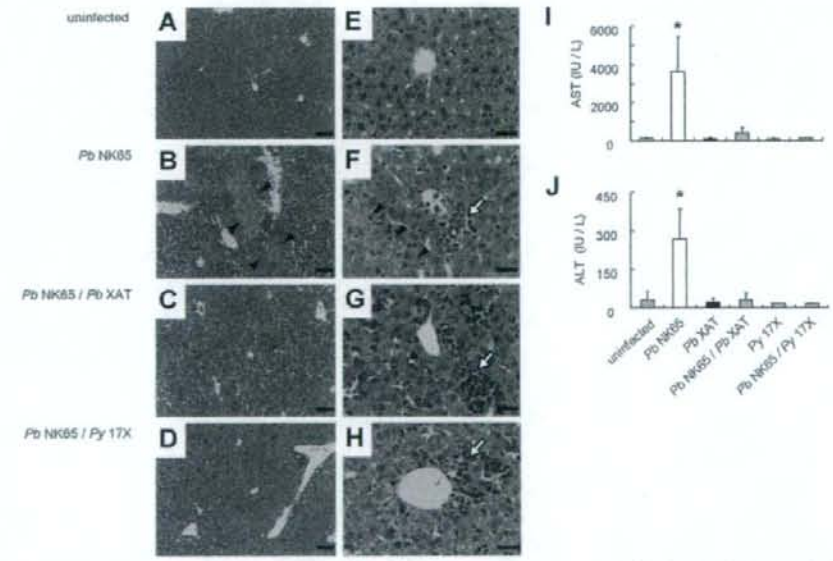

FIGURE 4. The existence of nonlethal malaria parasites prevents the liver injury caused by *Pb* NK65 infection. Mice were infected with malarial parasites as described in the legend to Fig. 2. Livers and plasma were obtained from infected mice on day 9 after infection and from uninfected mice. *A–H*, Histological analysis was performed after staining with H&E. Typical results of uninfected mice (*A* and *E*), mice singly infected with *Pb* NK65 (*B* and *F*), and mice coinfected with *Pb* NK65/*Pb* XAT (*C* and *G*) or *Pb* NK65/*Py* 17X (*D* and *H*) are shown. *A–D*, The scale bar indicates 100 μm. Arrowheads indicate focal necrosis of the liver cells. *E–H*, The scale bar indicates 40 μm. Arrows indicate dense infiltration of inflammatory cells. *I* and *J*, Levels of AST and ALT. Asterisks indicate a statistically significant difference (*, $p < 0.001$ as compared with uninfected control mice). Results are expressed as means ± SD of three mice. Experiments were performed three times with similar results and the representative data are shown.

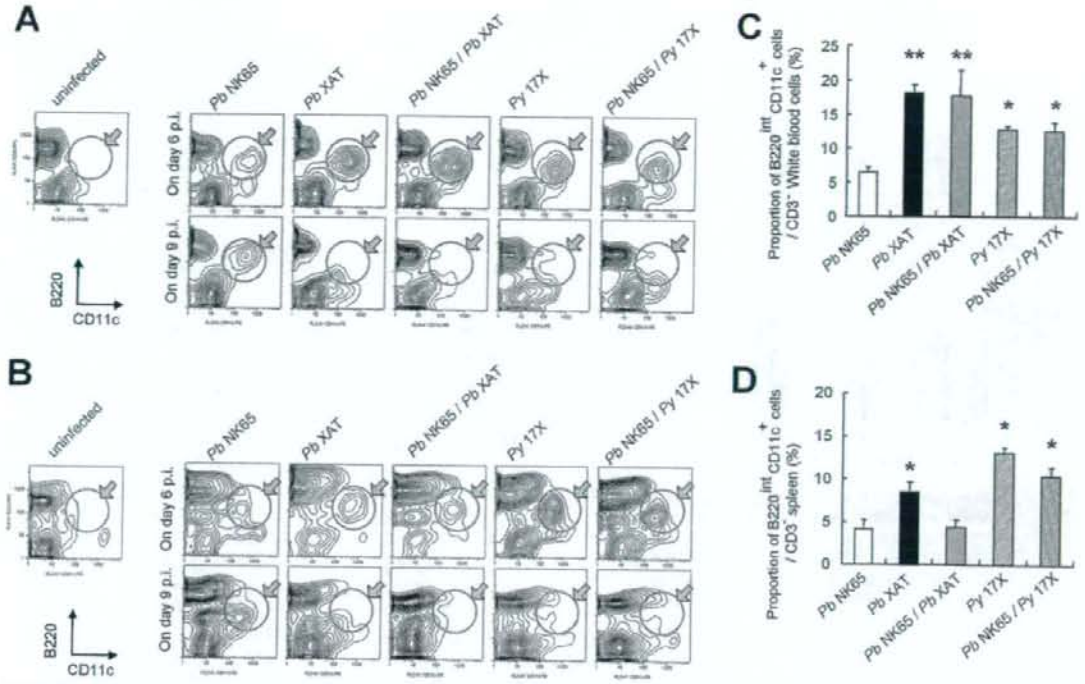

FIGURE 5. Coinfection with nonlethal parasites accelerates $B220^{int}CD11c^+$ cell expansion in spleen and peripheral blood. Peripheral blood and spleen were obtained from infected mice as described in the legend to Fig. 2 on days 6 and 9 after infection and from uninfected mice. Analyses of $CD11c^+$ cell population in peripheral blood (*A* and *C*) and spleen (*B* and *D*) from infected mice were performed by flow cytometery. Expression of B220 and CD11c was analyzed in the gate of $CD3^-$. *A* and *B*, Contour plots of $B220^{int}CD11c^+$ cell population (day 6, *upper panels*; day 9, *lower panels*). p.i., Post infection. Experiments were performed three times with similar results and the representative results are shown. *C* and *D*, The proportion of $B220^{int}CD11c^+$ cells in $CD3^-$ cells is shown (on day 6 postinfection). Asterisks indicate a statistically significant difference (*, $p < 0.005$; **, $p < 0.001$ as compared with *Pb* NK65-infected mice). Results are expressed as means ± SD of three mice.

single infection, respectively (Fig. 5*C*). The $B220^{int}CD11c^+$ cell population in those four groups of mice decreased on day 9 postinfection (Fig. 5*A*, *lower panels*). Although $B220^{int}CD11c^+$ cells in *Pb* NK65-infected mice also expanded on day 6 postinfection, they were much less than those in coinfected or nonlethal parasite-infected mice. The cell population in *Pb* NK65-infected mice further expanded on day 9 postinfection, when no other groups of mice showed the expansion (Fig. 5*A*). The $B220^{int}CD11c^+$ cell population of spleen showed a similar pattern to that of peripheral blood (Fig. 5*B*), but the proportion of the cells in *Pb* NK65/*Pb* XAT-infected mice was lower than that in *Pb* XAT-infected mice on day 6 postinfection (Fig. 5*D*). These results suggested that coinfection with nonlethal parasites accelerated much more $B220^{int}CD11c^+$ cell expansion than did *Pb* NK65 single infection during the early phase of infection.

Coinfection with nonlethal parasites induces $CD4^+$ T cell expansion in spleen

We analyzed the kinetics of $CD4^+$ T cell expansion in spleen during single and mixed infection (Fig. 6). Significant expansion of splenic $CD4^+$ T cells in *Pb* XAT- or *Py* 17X-infected mice was observed from day 9 postinfection. In contrast, *Pb* NK65-infected mice did not show the increased levels of $CD4^+$ T cells even on day 9 postinfection. Mice coinfected with *Pb* NK65/*Pb* XAT or *Pb* NK65/*Py* 17X had almost the same number of splenic $CD4^+$ T cells as did *Pb* XAT- or *Py* 17X-infected mice, respectively.

Enhanced levels of IL-10 mRNA during coinfection and nonlethal infection

IFN-γ and IL-10 have been shown to be associated with protection and exacerbation during *P. berghei* and *P. yoelii* malaria (17, 18).

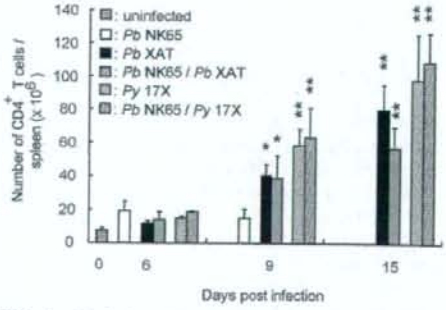

FIGURE 6. Coinfection with nonlethal parasites induces $CD4^+$ T cell expansion in spleen. Spleens were obtained from infected mice as described in the legend to Fig. 2 on days 6, 9, and 15 after infection and from uninfected mice. Splenic $CD3^+CD4^+$ cells were analyzed by flow cytometry and total numbers of $CD4^+$ T cells in spleen were calculated. Asterisks indicate a statistically significant difference (*, $p < 0.05$; **, $p < 0.005$ as compared with uninfected control mice). Results are expressed as means ± SD of three mice. Experiments were performed three times with similar results.

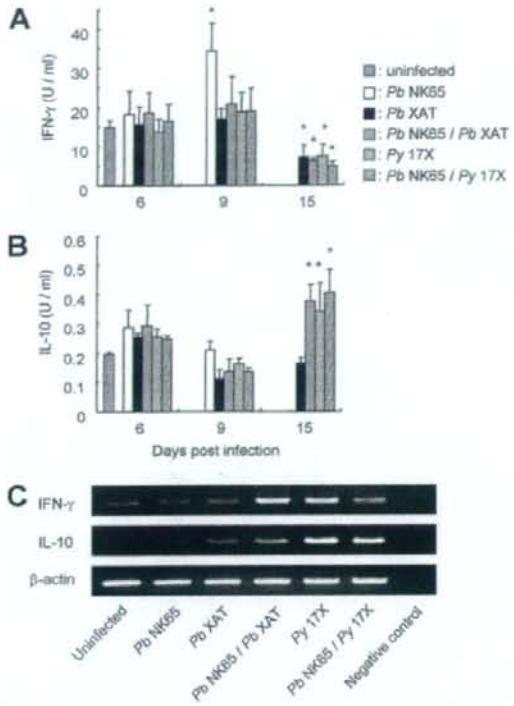

FIGURE 7. Enhanced levels of IL-10 mRNA during coinfection and nonlethal infection. *A* and *B*, Levels of IFN-γ or IL-10 were determined by ELISA. Plasma was collected from uninfected mice and infected mice on days 6, 9, and 15 post infection. *A*, Levels of IFN-γ in plasma. *B*, Levels of IL-10 in plasma. Asterisks indicate a statistically significant difference as compared with uninfected mice ($p < 0.001$). *C*, Total RNA was isolated from spleen of uninfected and infected mice as described in the legend to Fig. 2 on day 9 and subjected to RT-PCR using cytokine-specific primers. The samples without RNA template were used as negative control. Note that coinfected mice (*Pb* NK65/*Pb* XAT, *Pb* NK65/*Py* 17X) show IL-10 mRNA expression that is comparable to nonlethal parasite-infected mice (*Pb* XAT, *Py* 17X). Experiments were performed three times with similar results.

To examine whether these cytokines are associated with the suppression of *Pb* NK65-caused pathogenesis by coinfection with the nonlethal malaria parasites, we determined the levels of cytokines in plasma and cytokine mRNA in spleens from singly infected or coinfected mice (Fig. 7). *Pb* NK65 singly infected mice showed a high level of IFN-γ in plasma on day 9 compared with that in uninfected mice (Fig. 7*A*). Although the plasma IFN-γ levels in coinfected mice or nonlethal singly infected mice on days 6 and 9 were not different from those in uninfected mice, these mice showed significantly lower levels of IFN-γ than did uninfected mice on day 15. In contrast, strong IFN-γ mRNA expression was detected in the spleen from mice singly infected with *Py* 17X and coinfected with *Pb* NK65/*Pb* XAT and *Pb* NK65/*Py* 17X, compared with that observed in uninfected mice on day 9 (Fig. 7*C*). However, *Pb* NK65 singly infected mice did not show high levels of IFN-γ mRNA expression. These results suggested that spleen might not be a main organ for production of IFN-γ, which was involved in severe pathogenesis during *Pb* NK65 single infection (18), but the association of IFN-γ with suppressive pathogenesis by coinfection was still unclear.

The levels of IL-10 in plasma from single or coinfected mice on days 6 and 9 were not different from uninfected mice, but coinfected mice as well as nonlethal *Py* 17X singly infected mice showed elevated levels of IL-10 on day 15 (Fig. 7*B*). Although *Pb* NK65 singly infected mice showed only faint expression of IL-10 mRNA on day 9, mice coinfected with *Pb* NK65/*Pb* XAT or *Pb* NK65/*Py* 17X showed strong IL-10 mRNA expression, which was comparable to that observed in mice during *Pb* XAT or *Py* 17X single infection (Fig. 7*C*). IL-10 mRNA was not detected in spleen from uninfected mice. These results led us to hypothesize that the enhanced levels of IL-10 may be involved in suppression of pathogenesis during coinfection.

IL-10-deficient mice fail to receive benefits by coinfection with nonlethal malaria parasites

To examine whether IL-10 is associated with the suppression of the pathogenesis caused by coinfection, we determined the parasitemia, mortality, and the body weight of *Pb* NK65-infected IL-$10^{-/-}$ mice coinfected with *Pb* XAT or *Py* 17X. *Pb* NK65/*Pb* XAT-coinfected wild-type mice survived by day 21 (Fig. 8*D*), confirming the data obtained in Fig. 2*B*. In contrast, IL-$10^{-/-}$ mice coinfected with *Pb* NK65/*Pb* XAT began to die from day 10, and all mice died by day 21 postinfection (Fig. 8*D*) ($p = 0.034$). Moreover, their body weights were significantly lower than coinfected wild-type mice (Fig. 8*E*) ($p < 0.001$ on days 9, 11, and 13), although their parasitemia did not increase from day 11 (Fig. 8*F*). Similarly, *Pb* NK65/*Py* 17X-coinfected IL-$10^{-/-}$ mice began to die earlier than did wild-type mice (Fig. 8*G*), and their body weights were also lower than those of wild-type mice (Fig. 8*H*) ($p < 0.001$ on days 9, 13, and 18). During the period when coinfected IL-$10^{-/-}$ mice began to die, they developed liver injury (Fig. 8, *M* and *O*), which was not observed in coinfected wild-type mice (Fig. 8, *L* and *N*). In contrast, the parasitemia, mortality, the body weight, and development of liver injury of *Pb* NK65 singly infected IL-$10^{-/-}$ mice were not different from those of wild-type mice (Fig. 8, *A-C*, *J*, and *K*). Altogether, these results suggest that IL-10 may be involved in the suppressive effect of coinfection with nonlethal malaria parasites on the outcome of lethal *Pb* NK65 infection.

Discussion

In the present study, we investigated the influence of simultaneous infection with nonlethal murine malaria parasites, *Pb* XAT or *Py* 17X, on the outcome of the lethal *Pb* NK65 infection. *Pb* NK65 infection caused acute high parasitemia and pathogenesis, including body weight loss, severe anemia, and liver injury in mice. We found herein that the coinfection with nonlethal *Pb* XAT or *Py* 17X reduced such pathogenesis caused by *Pb* NK65 infection and prolonged survival of mice (Figs. 2–4). Because low levels of parasitemia and body weight loss in coinfected mice were observed from day 6 to 7 (Fig. 2), we postulated that T/B cell-mediated immunity would be involved in the suppressive effects of simultaneous infection with nonlethal parasites on lethal *Pb* NK65 infection and examined the response of dendritic cells and $CD4^+$ T cells.

The large expansion of $B220^{int}CD11c^+$ cells was observed in spleen and peripheral blood from coinfected mice on day 6, which was comparable to that from nonlethal parasite-infected mice (Fig. 5). These results suggest that expansion of $B220^{int}CD11c^+$ cells in coinfected mice may be accelerated by nonlethal parasite relative to lethal parasite infection. It has been reported that $CD11c^+$ dendritic cells are one of the professional APCs. As the murine plasmacytoid dendritic cell subset has been shown to coexpress CD11c and B220 (19–20), one would speculate that $B220^{int}CD11c^+$ cells expanded during nonlethal infection or coinfection might be one of the murine plasmacytoid dendritic cell subpopulations. Further characterization of the $B220^{int}CD11c^+$ cells, however, is needed for identification of these cells. In *Pb* NK65-infected mice, the peak expansion of $B220^{int}CD11c^+$ cells was observed on day 9, when these cells

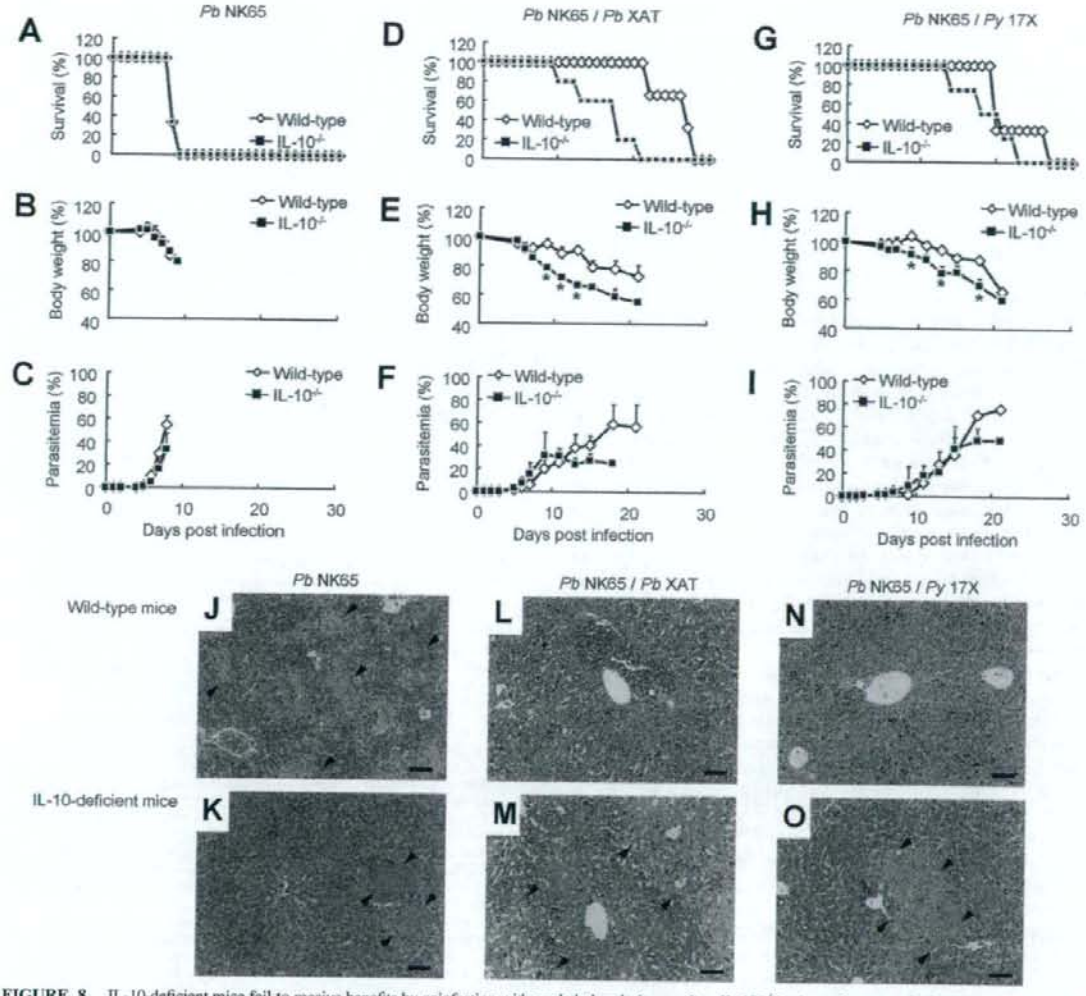

FIGURE 8. IL-10-deficient mice fail to receive benefits by coinfection with nonlethal malaria parasites. IL-$10^{-/-}$ mice and age-matched wild-type mice were singly infected with *Pb* NK65, coinfected with *Pb* NK65/*Pb* XAT, or coinfected with *Pb* NK65/*Py* 17X. Survival rates (*A*, *D*, and *G*), body weight (*B*, *E* and *H*), and course of parasitemia (*C*, *F*, and *I*) are shown. Asterisks indicate a statistically significant difference (*, $p < 0.001$ as compared with wild-type mice). Results are expressed as means ± SD of three to five mice. Histological analysis of liver was performed after staining with H&E (*J–O*). Livers were obtained from infected wild-type mice (*J*, *L*, and *N*) and IL-$10^{-/-}$ mice (*K*, *M*, and *O*) immediately after death from day 10 to 22 after infection. The scale bar indicates 100 μm. Arrowheads indicate focal necrosis of the liver cells. Experiments were performed twice with similar results and the representative data are shown.

began to decrease in coinfected mice as well as nonlethal *Pb* XAT- or *Py* 17X-infected mice. Because *Pb* NK65 parasites multiply quickly, especially in early phase of infection, earlier expansion of $B220^{int}CD11c^{+}$ cells may be the key for the suppression of pathogenesis during coinfection.

In contrast, mice coinfected with *Pb* NK65 and nonlethal *Pb* XAT or *Py* 17X showed increased levels of $CD4^{+}$ T cells from day 9 that were comparable to nonlethal parasite-infected mice (Fig. 6). Dendritic cells have been shown to activate naive T cells and play a crucial role in the initiation of immune responses (21–23). It is possible that the expansion of splenic $CD4^{+}$ T cells might be induced by $B220^{int}CD11c^{+}$ cells that had been expanded earlier (on day 6), and then the expanded $CD4^{+}$ T cells might be involved in suppression of pathogenesis in coinfected mice. $CD4^{+}$ T cells have been shown to play both protective and pathological roles during malaria infection (24–25). However, it seems that $CD4^{+}$ T cells would play protective roles during coinfection with lethal and nonlethal malaria parasites.

IL-10, which is produced by Th2 cells in $CD4^{+}$ T cell categories, inhibits inflammatory cytokines such as IFN-γ, TNF-α (26), and IL-12 (27). In malaria, IL-10 as well as TGF-β has been shown to be critical for host survival during *P. berghei* ANKA (28, 29) and *P. chabaudi* AS (30) infection. In the present study, *Pb* NK65/*Pb* XAT- or *Pb* NK65/*Py* 17X-coinfected mice showed high levels of IL-10 mRNA comparable to those in nonlethal *Pb* XAT- or *Py* 17X-infected mice (Fig. 7*C*), although *Pb* NK65-infected mice showed only a faint level of IL-10 mRNA. Moreover, high levels of IL-10 in plasma were followed by the IL-10 mRNA expression in coinfected mice on day 15 when IFN-γ production was

suppressed (Fig. 7). These results suggest that IL-10 may be involved in the suppression of pathogenesis in coinfected mice.

As expected, the suppressive effect of coinfection with nonlethal *Pb* XAT or *Py* 17X on severe body weight loss, liver injury, and mortality during *Pb* NK65 infection was reduced in IL-$10^{-/-}$ mice (Fig. 8), suggesting that IL-10 was involved in suppression of exacerbation of infection in simultaneous infection. The excessive inflammation has been shown to be able to account for body weight loss, liver injury, and mortality in mice infected with *Pb* NK65 (18, 31). Therefore, it is probable that enhancement of IL-10 would have suppressed the excessive inflammation caused by *Pb* NK65 and subsequently led to suppression of pathogenesis. In contrast, mortality as well as body weight loss in IL-$10^{-/-}$ mice during coinfection were not identical with those in *Pb* NK65 singly infected IL-$10^{-/-}$ mice, suggesting that other regulatory factors, such as TGF-β (30), may be involved in suppression of pathogenesis.

In the late phase of infection, IL-$10^{-/-}$ mice coinfected with *Pb* NK65/*Pb* XAT or *Pb* NK65/*Py* 17X had lower levels of parasitemia than that in wild-type mice. These results suggest that although IL-10 plays an important role for suppression of liver injury, it may be also involved in suppression of clearance of malaria parasites and cause death by severe anemia in the late phase of coinfection. It has been shown that during *Py* 17XL lethal infection, IL-10 is involved in the exacerbation of infection because depletion of IL-10 prolonged survival of hosts and made some mice resolve the infection (17, 32, 33). IL-10 might have dual roles, protective and pathological, in mice coinfected with lethal and nonlethal malaria parasites.

Our findings showing the beneficial influence of coinfection with nonlethal *Pb* XAT or *Py* 17X to hosts during *Pb* NK65 infection indicate that suppression of disease severity induced by coinfection occurs in not only cerebral malaria but also pathogenesis such as body weight loss and liver injury. Our data suggest that the beneficial influence of coinfection with nonlethal malaria parasites may not be species-specific because a different species of malaria parasites, *Py* 17X, also induced protective immunity to *Pb* NK65 lethal infection by simultaneous infection (Fig. 2). In endemic areas, coinfections have made diagnosis and treatment difficult because host immune responses induced by each of the different *Plasmodium* spp. are mutually interfered with in a complicated manner. Results obtained from in vivo models of coinfection with murine malaria parasites would contribute to understand the host immune responses during mixed infection with different *Plasmodium* spp.

Disclosures

The authors have no financial conflicts of interest.

References

1. Snow, R. W., M. H. Craig, U. Deichmann, and D. le Sueur. 1999. A preliminary continental risk map for malaria mortality among African children. *Parasitol. Today* 15: 99–104.
2. Breman, J. G. 2001. The ears of the hippopotamus: manifestations, determinants, and estimates of the malaria burden. *Am. J. Trop. Med. Hyg.* 64: 1–11.
3. Siribal, S., S. Nakasiri, S. Looareesuwan, and P. Chavalitshewinkoon-Petmitr. 2004. Identification of human malaria parasites and detection of mixed infection in Thai patients by nested PCR. *Southeast Asian J. Trop. Med. Public Health* 35: 5–9.
4. Imwong, M., S. Pukrittayakamee, A. C. Grüner, L. Rénia, F. Letourneur, S. Looareesuwan, N. J. White, and G. Snounou. 2005. Practical PCR genotyping protocols for *Plasmodium vivax* using *Pvcs* and *Pvmsp1*. *Malar. J.* 4: 20.
5. Mehlotra, R. K., K. Lorry, W. Kastens, S. M. Miller, M. P. Alpers, M. Bockarie, J. W. Kazura, and P. A. Zimmerman. 2000. Random distribution of mixed species malaria infections in Papua New Guinea. *Am. J. Trop. Med. Hyg.* 62: 225–231.
6. Pinto, J., C. A. Sousa, V. Gil, L. Gonçalves, D. Lopes, V. E. do Rosário, and J. D. Charlwood. 2000. Mixed-species malaria infections in the human population of São Tomé island, west Africa. *Trans. R. Soc. Trop. Med. Hyg.* 94: 256–257.
7. Ebrahimzadeh, A., B. Fouladi, and A. Fazaeli. 2007. High rate of detection of mixed infections of *Plasmodium vivax* and *Plasmodium falciparum* in south-east of Iran, using nested PCR. *Parasitol. Int.* 56: 61–64.
8. Mason, D. P., F. E. McKenzie, and W. H. Bossert. 1999. The blood-stage dynamics of mixed *Plasmodium malariae-Plasmodium falciparum* infections. *J. Theor. Biol.* 198: 549–566.
9. Mason, D. P., and F. E. McKenzie. 1999. Blood-stage dynamics and clinical implications of mixed *Plasmodium vivax-Plasmodium falciparum* infections. *Am. J. Trop. Med. Hyg.* 61: 367–374.
10. McQueen, P. G., and F. E. McKenzie. 2006. Competition for red blood cells can enhance *Plasmodium vivax* parasitemia in mixed-species malaria infections. *Am. J. Trop. Med. Hyg.* 75: 112–125.
11. Luxemburger, C., F. Ricci, F. Nosten, D. Raimond, S. Bathet, and N. J. White. 1997. The epidemiology of severe malaria in an area of low transmission in Thailand. *Trans. R. Soc. Trop. Med. Hyg.* 91: 256–262.
12. Snounou, G., T. Bourne, W. Jarra, S. Viriyakosol, J. C. Wood, and K. N. Brown. 1992. Assessment of parasite population dynamics in mixed infections of rodent plasmodia. *Parasitology* 105: 363–374.
13. Voza, T., A. M. Vigario, E. Belnoue, A. C. Gruner, J. C. Deschemin, M. Kayibanda, F. Delmas, C. J. Janse, B. Franke-Fayard, A. P. Waters, et al. 2005. Species-specific inhibition of cerebral malaria in mice coinfected with *Plasmodium* spp. *Infect. Immun.* 73: 4777–4786.
14. Mitchell, A. J., A. M. Hansen, L. Hee, H. J. Ball, S. M. Potter, J. C. Walker, and N. H. Hunt. 2005. Early cytokine production is associated with protection from murine cerebral malaria. *Infect. Immun.* 73: 5645–5653.
15. Waki, S., J. Tamura, M. Imanaka, S. Ishikawa, and M. Suzuki. 1982. *Plasmodium berghei*: isolation and maintenance of an irradiation attenuated strain in the nude mouse. *Exp. Parasitol.* 53: 335–340.
16. Kobayashi, F., M. Niikura, S. Waki, T. Matsui, T. Fujino, T. Tsuruhara, and S. Kamiya. 2007. *Plasmodium berghei* XAT: contribution of γδ T cells to host defense against infection with blood-stage nonlethal malaria parasite. *Exp. Parasitol.* 117: 368–375.
17. Kobayashi, F., T. Morii, T. Matsui, T. Fujino, Y. Watanabe, W. P. Weidanz, and M. Tsuji. 1996. Production of IL-10 during malaria caused by lethal and nonlethal variants of *Plasmodium yoelii yoelii*. *Parasitol. Res.* 82: 385–391.
18. Waki, S., S. Uehara, K. Kanbe, K. Ono, M. Suzuki, and H. Nariuchi. 1992. The role of T cells in pathogenesis and protective immunity to murine malaria. *Immunology* 75: 646–651.
19. Nakano, H., M. Yanagita, and M. D. Gunn. 2001. $CD11c^+B220^+Gr\text{-}1^+$ cells in mouse lymph nodes and spleen display characteristics of plasmacytoid dendritic cells. *J. Exp. Med.* 194: 1171–1178.
20. Bjorck, P. 2001. Isolation and characterization of plasmacytoid dendritic cells from Flt3 ligand and granulocyte-macrophage colony-stimulating factor-treated mice. *Blood* 98: 3520–3526.
21. Inaba, K., and R. M. Steinman. 1984. Resting and sensitized T lymphocytes exhibit distinct stimulatory (antigen-presenting cell) requirements for growth and lymphokine release. *J. Exp. Med.* 160: 1717–1735.
22. Knight, S. C., and A. J. Stagg. 1993. Antigen-presenting cell types. *Curr. Opin. Immunol.* 5: 374–382.
23. Metlay, J. P., M. D. Witmer-Pack, R. Agger, M. T. Crowley, D. Lawless, and R. M. Steinman. 1990. The distinct leukocyte integrins of mouse spleen dendritic cells as identified with new hamster monoclonal antibodies. *J. Exp. Med.* 171: 1753–1771.
24. Yoneto, T., T. Yoshimoto, C. R. Wang, Y. Takahama, M. Tsuji, S. Waki, and H. Nariuchi. 1999. Gamma interferon production is critical for protective immunity to infection with blood-stage *Plasmodium berghei* XAT but neither NO production nor NK cell activation is critical. *Infect. Immun.* 67: 2349–2356.
25. Langhorne, J., S. J. Meding, K. Eichmann, and S. S. Cillard. 1989. The response of $CD4^+$ T cells to *Plasmodium chabaudi chabaudi*. *Immunol. Rev.* 112: 71–94.
26. Mosmann, T. R., and K. W. Moore. 1991. The role of IL-10 in crossregulation of TH1 and TH2 responses. *Immunol. Today* 12: A49–A53.
27. Xu, X., K. Sumita, C. Feng, X. Xiong, H. Shen, S. Maruyama, M. Kanoh, and Y. Asano. 2001. Down-regulation of IL-12 p40 gene in *Plasmodium berghei*-infected mice. *J. Immunol.* 167: 235–241.
28. Tan, R. S., A. U. Kara, C. Feng, Y. Asano, and R. Sinniah. 2000. Differential IL-10 expression in interferon regulatory factor-1 deficient mice during *Plasmodium berghei* blood-stage infection. *Parasite Immunol.* 22: 425–435.
29. Kossodo, S., C. Monso, P. Juillard, T. Velu, M. Goldman, and G. E. Grau. 1997. Interleukin-10 modulates susceptibility in experimental cerebral malaria. *Immunology* 91: 536–540.
30. Li, C., L. A. Sanni, F. Omer, E. Riley, and J. Langhorne. 2003. Pathology of *Plasmodium chabaudi chabaudi* infection and mortality in IL-10-deficient mice are ameliorated by anti-tumor necrosis factor α and exacerbated by anti-transforming growth factor β antibodies. *Infect. Immun.* 71: 4850–4856.
31. Yoshimoto, T., Y. Takahama, C. R. Wang, T. Yoneto, S. Waki, and H., Nariuchi. 1998. A pathogenic role of IL-12 in blood-stage murine malaria lethal strain *Plasmodium berghei* NK65 infection. *J. Immunol.* 160: 5500–5505.
32. Omer, F. M., J. B. de Souza, and E. M. Riley. 2003. Differential induction of TGF-β regulates proinflammatory cytokine production and determines the outcome of lethal and nonlethal *Plasmodium yoelii* infections. *J. Immunol.* 171: 5430–5436.
33. Kobayashi, F., H. Ishida, T. Matsui, and M. Tsuji. 2000. Effects of in vivo administration of anti-IL-10 or anti-IFN-γ monoclonal antibody on the host defense mechanism against *Plasmodium yoelii yoelii* infection. *J. Vet. Med. Sci.* 6: 583–587.

Structures of *Trypanosoma cruzi* Dihydroorotate Dehydrogenase Complexed with Substrates and Products: Atomic Resolution Insights into Mechanisms of Dihydroorotate Oxidation and Fumarate Reduction

Daniel Ken Inaoka, Kimitoshi Sakamoto, Hironari Shimizu, Tomoo Shiba, Genji Kurisu, Takeshi Nara, Takashi Aoki, Kiyoshi Kita, and Shigeharu Harada

Department of Biomedical Chemistry, Graduate School of Medicine, The University of Tokyo, Tokyo 113-0033, Japan, Department of Life Sciences, Graduate School of Arts and Sciences, The University of Tokyo, Tokyo 153-8902, Japan, Department of Molecular and Cellular Parasitology, Juntendo University, Tokyo 113-8421, Japan, and Department of Applied Biology, Graduate School of Science and Technology, Kyoto Institute of Technology, Kyoto 606-8585, Japan

Biochemistry®

Reprinted from
Volume 47, Number 41, Pages 10881–10891

Structures of *Trypanosoma cruzi* Dihydroorotate Dehydrogenase Complexed with Substrates and Products: Atomic Resolution Insights into Mechanisms of Dihydroorotate Oxidation and Fumarate Reduction[†,‡]

Daniel Ken Inaoka,[§,||] Kimitoshi Sakamoto,[§] Hironari Shimizu,[§] Tomoo Shiba,[⊥] Genji Kurisu,[⊥] Takeshi Nara,[#] Takashi Aoki,[#] Kiyoshi Kita,[*,§] and Shigeharu Harada[*,○]

Department of Biomedical Chemistry, Graduate School of Medicine, The University of Tokyo, Tokyo 113-0033, Japan, Department of Life Sciences, Graduate School of Arts and Sciences, The University of Tokyo, Tokyo 153-8902, Japan, Department of Molecular and Cellular Parasitology, Juntendo University, Tokyo 113-8421, Japan, and Department of Applied Biology, Graduate School of Science and Technology, Kyoto Institute of Technology, Kyoto 606-8585, Japan

Received March 11, 2008; Revised Manuscript Received July 25, 2008

ABSTRACT: Dihydroorotate dehydrogenase (DHOD) from *Trypanosoma cruzi* (TcDHOD) is a member of family 1A DHOD that catalyzes the oxidation of dihydroorotate to orotate (first half-reaction) and then the reduction of fumarate to succinate (second half-reaction) in the *de novo* pyrimidine biosynthesis pathway. The oxidation of dihydroorotate is coupled with the reduction of FMN, and the reduced FMN converts fumarate to succinate in the second half-reaction. TcDHOD are known to be essential for survival and growth of *T. cruzi* and a validated drug target. The first-half reaction mechanism of the family 1A DHOD from *Lactococcus lactis* has been extensively investigated on the basis of kinetic isotope effects, mutagenesis and X-ray structures determined for ligand-free form and in complex with orotate, the product of the first half-reaction. In this report, we present crystal structures of TcDHOD in the ligand-free form and in complexes with an inhibitor, physiological substrates and products of the first and second half-reactions. These ligands bind to the same active site of TcDHOD, which is consistent with the one-site ping-pong Bi-Bi mechanism demonstrated by kinetic studies for family 1A DHODs. The binding of ligands to TcDHOD does not cause any significant structural changes to TcDHOD, and both reduced and oxidized FMN cofactors are in planar conformation, which indicates that the reduction of the FMN cofactor with dihydroorotate produces anionic reduced FMN. Therefore, they should be good models for the enzymatic reaction pathway of TcDHOD, although orotate and fumarate bind to TcDHOD with the oxidized FMN and dihydroorotate with the reduced FMN in the structures determined here. Cys130, which was identified as the active site base for family 1A DHOD (Fagan, R. L., Jensen, K. F., Bjornberg, O., and Palfey, B. A. (2007) *Biochemistry 46*, 4028–4036.), is well located for abstracting a proton from dihydroorotate C5 and transferring it to outside water molecules. The bound fumarate is in a twisted conformation, which induces partial charge separation represented as $C_2^{\delta-}$ and $C_3^{\delta+}$. Because of this partial charge separation, the thermodynamically favorable reduction of fumarate with reduced FMN seems to proceed in the way that $C_2^{\delta-}$ accepts a proton from Cys130 and $C_3^{\delta+}$ a hydride (or a hydride equivalent) from reduced FMN N_5 in TcDHOD.

Dihydroorotate dehydrogenase (DHOD[1]) is a flavoenzyme that catalyzes oxidation of (*S*)-dihydroorotate to orotate, the fourth step and the only redox reaction in the *de novo* pyrimidine biosynthesis pathway (Figure S1, Supporting Information). In the first half-reaction, oxidation of dihydroorotate is coupled with reduction of a flavin mononucleotide (FMN) cofactor. Based on amino acid sequence similarity, DHODs from different organisms can be divided into two families, family 1 and family 2 (*1*). Family 1 DHODs are cytoplasmic enzymes and can be further subdivided into families 1A and 1B. Family 1A enzymes

[†] This work was supported by grants to S.H. and K.K. from the Targeted Proteins Research Program (TPRP), Japan Aerospace Exploration Agency (JAXA), and in part by Grant-in-Aid for Scientific Research on Priority Areas, for the 21st Century COE Program and Creative Scientific Research from the Japanese Ministry of Education, Culture, Sports and Technology, and for Scientific Research (B) from Japan Society for the Promotion of Science. D.K.I. was a research fellow supported by Japan Society for the Promotion of Science.

[‡] Protein Data Bank coordinates and structure factors have been deposited as entries 2DJX for ligand-free TcDHOD, 2E6F for TcDHOD−oxonate, 2E68 for TcDHOD−dihydroorotate, 2E6A for TcDHOD−orotate, 2E6D for TcDHOD−fumarate and 2DJL for TcDHOD−succinate complexes.

* To whom correspondence should be addressed. K.K.: 7-3-1 Hongo, Bunkyo-ku, Tokyo 113-0033, Japan. Fax: (+81)-3-5841-3526. E-mail: kitak@m.u-tokyo.ac.jp. S.H.: Gosyokaidou-cho, Matsugasaki, Sakyo, Kyoto 606-8585, Japan. Fax: (+81)-75-724-7541. E-mail: harada@kit.ac.jp.

[§] Graduate School of Medicine, The University of Tokyo. Tel: +81-3-5841-3528.

[||] E-mail: danielken@m.u-tokyo.ac.jp.

[⊥] Graduate School of Arts and Sciences, The University of Tokyo.

[#] Juntendo University.

[○] Kyoto Institute of Technology. Tel: +81-75-724-7541.

[1] Abbreviations: DHOD, dihydroorotate dehydrogenase; FMN, flavin mononucleotide; FAD, flavin adenine dinucleotide; NAD, nicotinamide adenine dinucleotide; MWCO, molecular weight cutoff.

10.1021/bi800413r CCC: $40.75
Published on Web 09/23/2008

form homodimers and appear to utilize fumarate as a physiological oxidant, in conjunction with oxidation of the reduced FMN cofactor during the second half-reaction (*1*). In contrast, family 1B enzymes form heterotetramers and utilize NAD^+ via a distinct protein subunit that contains a 2Fe-2S cluster and FAD cofactor (*1*). Members of family 2 exist as homodimers or monomers and are membrane-bound enzymes that utilize respiratory quinone as a physiological oxidant during the second half-reaction (*2*−*4*). The N-terminal domain found only in family 2 DHODs forms the binding site for quinone (*5*).

Many inhibitors targeting the quinone binding-site have been designed such as human DHOD inhibitor leflunomide that is in clinical use to treat rheumatoid arthritis (*5*). Other potent and selective inhibitors designed for family 2 DHODs from *Escherichia coli* (*6*), *Helicobacter pylori* (*7*) and *Plasmodium falciparum* (*2*, *8*, *9*) inhibit their growth. These inhibitors designed for family 2 DHODs are not effective against family 1A DHODs, since family 1A lacks the quinone binding site. On the other hand, hydroxybenzoates such as 3,4-dihydroxybenzoate and 3,5-dihydroxybenzoate are inhibitors specific for family 1A DHODs (*10*, *11*), although these inhibitors with IC_{50}s in the range of micromolar order are not potent. Previously, we reported the organization and amino acid sequences of all enzymes in the *de novo* pyrimidine biosynthesis pathway of *Trypanosoma cruzi* (*12*). In that work, we found that the *T. cruzi pyr4* gene product is homologous to family 1A DHODs from *Lactococcus lactis* and *Saccharomyces cerevisiae*. DHOD from *T. cruzi* (TcDHOD) is 313 amino acids in length (Figure 1) and exists in cells as a homodimer (MW 2 × 34 kDa). In addition to DHOD activity, TcDHOD also shows fumarate reductase activity, suggesting that it is involved not only in the *de novo* pyrimidine biosynthesis pathway but also in redox homeostasis of the parasite (*12*−*14*). Recently, Annoura et al. (*15*) demonstrated that TcDHOD knockout *T. cruzi* could not survive even in the presence of substrates for enzymes of pyrimidine salvage pathway. The importance of DHOD to survival of *Trypanosoma brucei* in the blood stream form was also shown by Arakaki et al. (*16*). Therefore, the enzyme has the characteristics of a promising target for the development of chemotherapeutic agents to combat infections with the pathogen.

To date, X-ray structure analyses have been performed for seven DHODs from six organisms: family 1A DHODs from *L. lactis* (*17*) and *T. brucei* (*16*), family 1B DHOD from *L. lactis* (*18*), and family 2 DHODs from *E. coli* (*4*), *P. falciparum* (*19*), *Rattus rattus* (*20*) and *Homo sapiens* (*5*). Although kinetic studies of the catalytic mechanism for DHOD have extensively been performed (*21*−*30*), none of the structures determined to date include DHOD in a complex with a physiological substrate. In this study, we determined the crystal structures of TcDHOD in the ligand-free form, in complexes with substrates and products of the first and second half-reactions, and in a complex with an inhibitor, oxonate at atomic resolution. These structures, in particular those of TcDHOD complexed with dihydroorotate and fumarate, provided us further insights into the catalytic mechanisms of dihydroorotate oxidation and fumarate reduction.

EXPERIMENTAL PROCEDURES

Cloning, Expression and Purification. Recombinant TcDHOD was expressed, purified and crystallized as previously reported (*31*). Briefly, TcDHOD was purified to homogeneity using DEAE Fast Flow (GE Healthcare) followed by Phenyl Sepharose H.P. (GE Healthcare) and TSK G3000SW (Tosoh). A total of 11 mg of TcDHOD with high specific activity (12.5 μmol/min/mg) was purified from 10 L of culture (Table S1, Supporting Information). The addition of 0.25 mM orotate during purification and storage was indispensable to stabilize the enzymatic activity.

Protein Assay and FMN Content Determination. Protein concentrations were determined according Lowry with bovine serum albumin as the standard (*32*). The FMN content of the purified TcDHOD was estimated to be 1.0 using a spectroscopic method, on the basis of the extinction coefficient of FMN (11.1 mM^{-1} cm^{-1} at 450 nm).

Enzyme Assay. DHOD activity was measured as described previously (*14*) with minor modifications. Orotate production was assayed by measuring the absorption at 290 nm (ε = 6.4 × mM^{-1} × cm^{-1}). The reaction was started by adding 0.5 mM dihydroorotate into the reaction mixture containing 50 mM potassium phosphate buffer pH 7.5, 2 mM sodium fumarate and TcDHOD in a final volume of 1 mL.

Crystallization. The plate-shaped dark-orange crystals of the TcDHOD−orotate complex with the oxidized FMN cofactor were obtained at 277 K by the hanging drop vapor diffusion method using 16% (w/v) PEG 3350, 100 mM sodium cacodylate pH 6.2, 1 mM sodium orotate, 50 mM hexaamminecobalt (III) chloride and 1 mM sodium thiocyanate as the reservoir solution (*31*). The TcDHOD−oxonate complex was prepared by repeated concentration and dilution of the purified enzyme with a buffer containing oxonate using an Amicon Ultra-4 10,000 MWCO filter. This was followed by cocrystallization in a similar manner as described above except that cocrystallization was carried out in the presence of 1 mM oxonate instead of orotate at pH 5.1. Crystals of the ligand-free TcDHOD were prepared by back-soaking crystals of the TcDHOD−oxonate complex in buffer A (100 mM cacodylate pH 5.1, 20% (w/v) polyethylene glycol 3350, 50 mM hexaamminecobalt (III) chloride and 1 mM sodium thiocyanate) for three days with repeated buffer exchange. Crystals of the TcDHOD−succinate and −fumarate complexes were prepared by soaking ligand-free crystals for three days in buffer A containing 10 mM succinate or fumarate, respectively. Crystals of the TcDHOD−dihydroorotate complex were obtained by soaking ligand-free crystals for 10 to 15 s in buffer A containing 10 mM dihydroorotate plus 15% (w/v) glycerol. During soaking, the color of the crystals changed from dark to light orange, which indicates that the FMN cofactor was reduced by dihydroorotate. After soaking, a crystal mounted in a nylon loop was immediately flash-frozen in a nitrogen stream at 100 K, and X-ray diffraction data were collected. During data collection, the light orange color of the crystals was kept. Since kinetic analysis indicated that dihydroorotate can be bound to TcDHOD with the reduced FMN cofactor if an excess amount of dihydroorotate is present (*14*, *26*), the crystals prepared should be those of the TcDHOD−dihydroorotate complex with the reduced FMN cofactor.

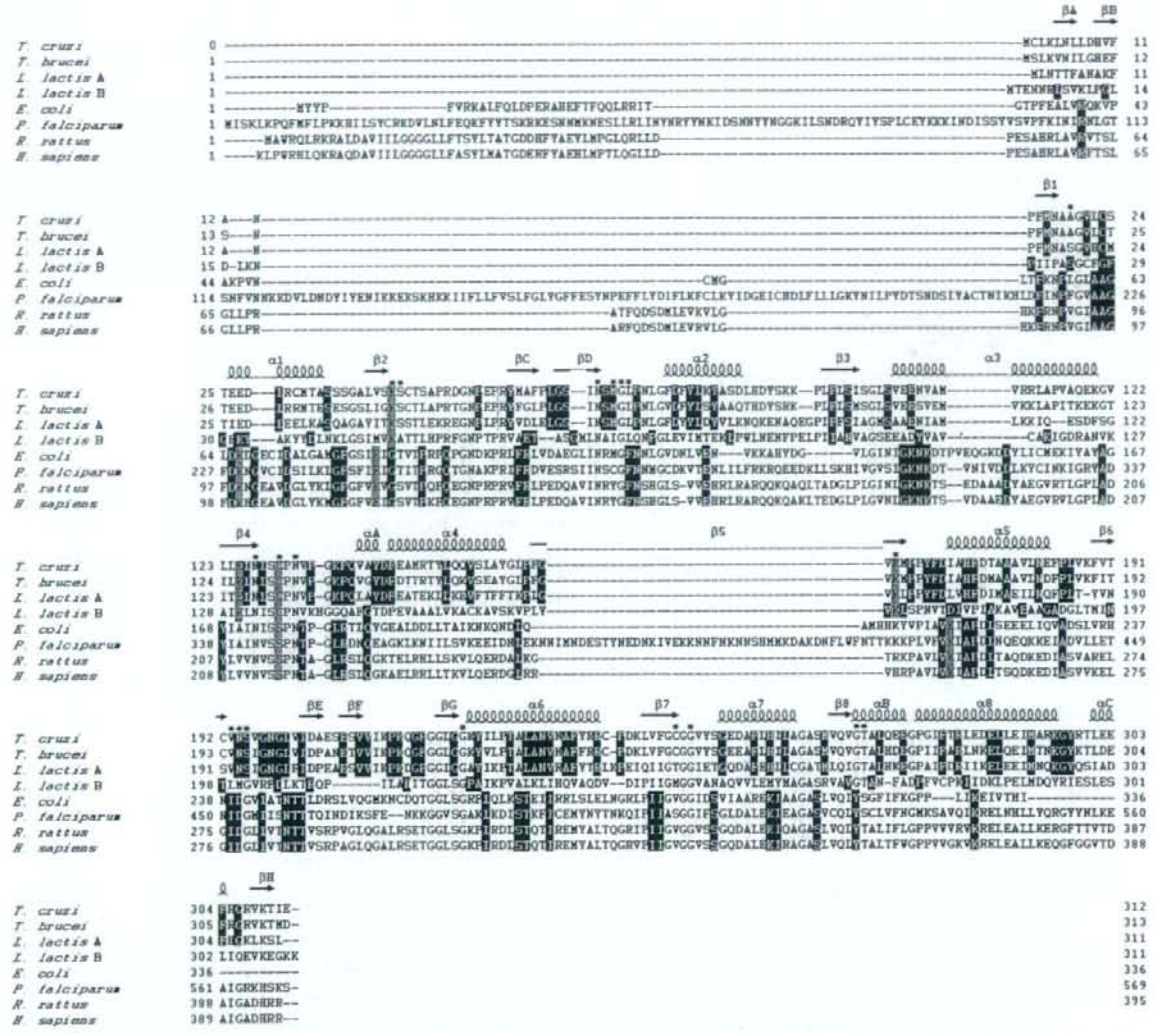

FIGURE 1: Multiple alignment of amino acid sequences of DHODs. The alignment was produced from fourteen amino acid sequences from family 1A (*T. cruzi*/AB212956.1, *T. brucei*/AC159455.1, *L. lactis*/X74206.1, *Streptococcus pneumoniae*/ABJ54983.1 and *Saccharomyces kluyveri*/AY323902.1), catalytic subunit of family 1B (*L. lactis*/CAA52280.1, *Streptococcus thermophilus*/AAV62538.1, *Enterococcus faecalis*/AAO81490, *Clostridium tetani*/AAO36852.1 and *Clostridium cellulolyticum*/ZP_01576243.1) and family 2 (*E. coli*/CAA26594.1, *P. falciparum*/CAG25203.1, *R. rattus*/CAA56765.1 and *H. sapiens*/AAA50163.1) DHODs using CLUSTAL-W. Alignment of eight DHODs, whose structures are known, is shown. They belong to family 1A (*T. cruzi*, *T. brucei* and *L. lactis* A), family 1B (*L. lactis* B) or family 2 (*E. coli*, *P. falciparum*, *R. rattus* and *H. sapiens*). Their PDB codes are 2DJX (this study), 2B4G (*16*), 2DOR (*29*), 1EP2 (*18*), 1F76 (*4*), 1TV5 (*19*), 1UUO (*20*) and 1D3G (*5*), respectively. In yellow, residues conserved in more than one family. In red, those conserved only within a family. Secondary structural elements of the TcDHOD structure are also indicated; β strands are shown as arrows and α helices as squiggles. Residues involved in interactions with FMN, oxonate, dihydroorotate, orotate, fumarate or succinate are marked with an asterisk. TcDHOD Lys43, Glu125, Cys130 and Lys164, which are mentioned in Discussion, along with their structurally equivalent residues in other DHODs, are colored blue. The numbers shown for amino acid residues of the TcDHOD protein referred to those of *L. lactis* DHODA.

X-ray Data Collection, Phasing and Refinement. X-ray diffraction data sets for TcDHOD in the ligand-free form and in complexes with orotate, fumarate and succinate were collected at 100 K with beamline BL44XU from SPring-8 (λ = 0.900 Å) in Harima, Japan, using a Bruker AXS DIP6040 detector. Data sets for TcDHOD−oxonate and −dihydroorotate complexes were collected at 100 K with beamline NW12 of Photon Factory Advanced Ring (λ = 1.000 Å) in Tsukuba, Japan, using an ADSC Quantum-210 detector. All data sets were indexed, integrated and scaled using *HKL2000* (*33*). Table 1 summarizes data collection statistics. The structure of the TcDHOD−orotate complex was solved by the molecular replacement method using *Molrep* (*34*). A search model was generated from a single monomer of the *L. lactis* DHODA dimer structure (PDB code, 2DOR; 55% sequence identity with TcDHOD) with all non-protein atoms removed. The sequence was changed to that of TcDHOD by applying the TcDHOD sequence (NCBI accession number BAE48283 (*35*)) onto the search model using Swiss-Pdb Viewer (*36*). The molecular replace-

Table 1: Data Collection and Refinement Statistics[a]

	ligand-free	oxonate	dihydroorotate	orotate	fumarate	succinate
			Data Collection			
space group	$P2_12_12_1$	$P2_12_12_1$	$P2_12_12_1$	$P2_12_12_1$	$P2_12_12_1$	$P2_12_12_1$
cell dimensions						
a, *b*, *c* (Å)	69.96, 73.13, 126.09	68.36, 71.83, 123.64	68.44, 71.94, 123.85	68.25, 71.88, 123.57	68.28, 71.88, 123.61	68.15, 71.77, 123.40
wavelength (Å)	0.9	1.0	1.0	0.9	0.9	0.9
resolution (Å)	50.0−1.58 (1.64−1.58)	50.0−1.26 (1.29−1.26)	50.0−1.38 (1.43−1.38)	50.0−1.64 (1.70−1.64)	50.0−1.94 (2.01−1.94)	50.0−1.38 (1.43−1.38)
R_{merge} (%)	7.0 (39.8)	7.1 (39.5)	8.4 (39.6)	7.8 (39.8)	9.9 (24.4)	6.0 (33.0)
$I/\sigma(I)$	8.2 (2.76)	8.5 (3.04)	10.5 (4.26)	9.9 (3.12)	12.8 (8.19)	9.0 (2.62)
completeness (%)	98.5 (99.4)	97.7 (99.2)	97.5 (98.9)	96.1 (97.9)	99.9 (100.0)	94.9 (69.5)
redundancy	4.0	4.4	4.6	3.7	6.1	5.2
			Refinement			
resolution (Å)	40.0−1.58	30.0−1.26	30.0−1.38	50.0−1.64	50.0−1.94	50.0−1.38
no. of reflections	86263	152389	116503	68521	43381	112910
R-factor/*R*-free	0.182/0.204	0.166/0.180	0.169/0.183	0.164/0.192	0.158/0.200	0.166/0.183
no. of atoms						
protein	4758	4758	4758	4758	4758	4758
FMN	31	31	31	31	31	31
ligand	0	22	22	22	16	16
water	689	799	637	497	476	696
B-factors						
protein	17.1	9.9	12.0	10.7	9.7	12.0
FMN	11.5	5.7	4.5	6.1	5.1	7.4
ligand		6.8	7.4	5.6	11.8	9.6
water	25.0	19.6	18.0	20.9	17.5	21.2
rms deviations						
bond lengths (Å)	0.009	0.007	0.008	0.011	0.015	0.007
bond angles (deg)	1.219	1.171	1.219	1.309	1.438	1.192

[a] Highest-resolution shell is shown in parentheses.

ment was carried out under different resolution ranges of 2.0−8.0, 3.0−8.0 and 4.0−8.0 Å. Essentially consistent solutions giving one TcDHOD dimer in the asymmetric unit were obtained. The resulting model obtained after rigid-body refinement was refined at 2.5 Å resolution under strict noncrystallographic symmetry (NCS) restraints using *CNS* (*37*), and electron-density maps calculated with σ_A-weighted $2F_o - F_c$ and $F_o - F_c$ coefficients were generated and inspected to check the validity of the initial model. After a few rounds of refinement and manual rebuilding using *CNS* and *Coot* (*38*), respectively, FMN cofactors and orotate molecules became clearly visible on electron-density maps and were incorporated into the model. Subsequently, the model was subjected to iterative cycles of refinement and manual rebuilding at 1.64 Å resolution using isotropic temperature factors and weak NCS restraints. At this stage, many water molecules were identified using electron-density maps (3σ cutoff). The model was finally refined using *Refmac5* (*39*) and *Coot* without NCS restraints, resulting in *R*-factor and *R*-free values of 0.164 and 0.192, respectively. In the final homodimer model of the TcDHOD−orotate complex, each subunit consists of 312 amino acid residues from Met0 to Ile311, one oxidized FMN cofactor and one orotate molecule. The C-terminal amino acid residue, Glu312, could not be defined on the final $2F_o - F_c$ electron density map. In the Ramachandran plot (*40*), 93.2% of the residues are in the most favored regions and 6.8% are in additionally allowed regions, as defined by *PROCHECK* (*41*). The structures of the ligand-free TcDHOD and the complexes with dihydroorotate, oxonate, fumarate and succinate were refined starting from the protein atom coordinates of the TcDHOD−orotate complex. Coordinate files and appropriate restrains for those ligands were generated using the PRODRG server and Sketcher program of the CCP4 suite (*42*).

Successful preparations of crystals of the ligand-free TcDHOD and those of TcDHOD in complexes with dihydroorotate, fumarate and succinate were confirmed by inspecting $2F_o - F_c$ electron density maps calculated after omit refinement (Figure S2 A−L, Supporting Information). In the map calculated for the ligand-free TcDHOD (Figure S2 A, B), four water molecules located near the FMN isoalloxazine ring in the active site were assigned. Well-shaped electron dense regions corresponding to dihydroorotate, fumarate or succinate were also recognized in the active site of each complex. Refinement statistics for all models are summarized in Table 1.

RESULTS

Overall Structure. In the presence of orotate, the TcDHOD protein, consisting of 313 amino acid residues and one oxidized FMN cofactor, was crystallized in orthorhombic space group $P2_12_12_1$ with two identical subunits related by a noncrystallographic 2-fold axis present in the crystallographic asymmetric unit. Crystals of the ligand-free TcDHOD and of TcDHOD in complexes with the substrates (dihydroorotate and fumarate), products (orotate and succinate) and the inhibitor (oxonate) were prepared as described in Experimental Procedures. Crystals of TcDHOD−dihydroorotate complex included the reduced FMN cofactor, but the other five crystal forms included the oxidized FMN cofactor. All structures determined included a 312 amino acid region from Met0 to Ile311 of the full-length protein but the C-terminal Glu312 was not assigned. Figure 1 shows a multiple amino acid sequence alignment of TcDHOD and

FIGURE 2: Structure of ligand-free TcDHOD (stereo views). (A) Ribbon diagram of the TcDHOD subunit structure. The $(\alpha/\beta)_8$ barrel is represented in blue (α-helices) and magenta (β-strands); the $\beta4-\alpha A$ loop, the active site loop, is shown in gray; and the FMN cofactor is shown in yellow. The color code for each atom type is as follows: red, oxygen; blue, nitrogen; orange, phosphate. The same color-code was applied to all figures. (B) The dimer structure viewed from above the 2-fold axis. The $(\alpha/\beta)_8$ barrel of each subunit is color-coded as described in (A). The $\beta6-\alpha6$ loops, helices α6 and α7, which participate in dimer interface interactions, are in red. Arrows indicate intersubunit salt bridges between Glu207 and Lys296, shown in yellow. The images were generated using PyMOL (http://pymol.sourceforge.net).

seven DHODs with known structures. Figures 2A and 2B show the subunit and homodimer structures of the ligand-free TcDHOD. As there are no significant differences between the structures of the two subunits, as indicated by a root-mean-square (rms) deviation of 0.20 Å calculated for superimposed 312 C_α positions, we will instead focus on one subunit to describe the structure as a whole.

The overall structure of TcDHOD is very similar to those of other DHODs listed in Figure 1. The C_α atoms of a TcDHOD subunit can be superimposed on the structurally equivalent 311 C_α atoms of *T. brucei* DHOD (PDB code, 2B4G) or the 298 C_α atoms of *L. lactis* DHODA (2DOR) with rms deviations of 0.39 and 0.82 Å, respectively, which indicates that the main-chain structures of these three DHODs, especially TcDHOD and *T. brucei* DHOD, are essentially identical. The rms deviations for DHODs from different families are somewhat larger; namely, for the family 1B member *L. lactis* DHODB (1EP2), rms deviation of 1.94 Å for 270 C_α atoms and for family 2 members, as follows, 1.76 Å for 253 C_α atoms of *E. coli* DHOD (1F76), 1.68 Å for 275 C_α atoms of *P. falciparum* DHOD (1TV5), 1.81 Å for 186 C_α atoms of *R. rattus* DHOD (1UUO) and 1.74 Å for 272 C_α atoms of *H. sapiens* DHOD (1D3G). In addition, the dimer structure of DHOD from *T. cruzi* Y strain, in which TcDHOD Phe61 is replaced by a valine residue, was determined at 2.2 Å resolution as a form with a sulfate ion bound to its active site (*(43)*; PDB code 3C3N), during the submission of this article. TcDHOD is very similar to 3C3N as indicated by the rms deviation of 0.44 Å.

As is true for the many other flavin containing proteins, TcDHOD subunits fold into an $(\alpha/\beta)_8$ motif with a parallel eight-stranded β-barrel ($\beta1-\beta8$) surrounded by eight α-helices ($\alpha1-\alpha8$), with the FMN cofactor on the C-terminal end of the β-barrel. Each of the secondary structural elements of the $(\alpha/\beta)_8$ motif is connected to the next one via a short loop consisting of several amino acid residues. The loops

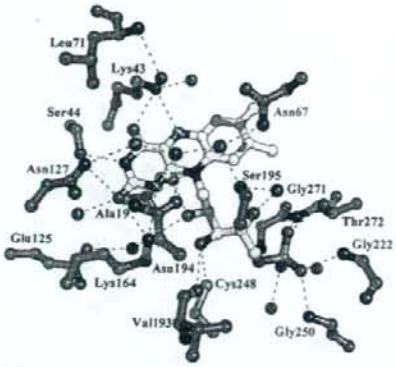

FIGURE 3: The environment of the FMN cofactor of the ligand-free TcDHOD. Amino acid residues and the FMN cofactor are indicated by green or yellow ball-and-stick models, respectively, and ten water molecules (A−J) that were assigned in this region are also shown. Hydrogen bonds are represented by dotted lines. Residue names shown by red are conserved in the amino acid sequences of all known DHODs. The images were generated using PyMOL (http://pymol.sourceforge.net).

connecting β2 and α2 (β2−α2 loop, residues 43−75), β4 and α4 (β4−α4 loop, residues 128−142) and β6 and α6 (β6−α6 loop, residues 193−222) are longer than the others and include additional secondary structural elements. Moreover, in each subunit, βC, βD in the β2−α2 loop and βG in the β6−α6 loop form a three-stranded antiparallel β-sheet, whereas βE and βF in the β6−α6 loop form a two-stranded antiparallel β-sheet (Figure 2A). In the dimer structure, the β6−α6 loop protrudes from one subunit toward α6 and α7 of the other, forming dimer interfaces. Each interface includes an intersubunit three-stranded β-sheet composed of βE and βF of one subunit plus βH of the other, and an intersubunit salt bridge between Glu207 and Lys296 (Figure 2B). Additionally, hydrophobic interactions occur between subunits.

The FMN cofactor is well buried except for a partially exposed dimethyl benzene moiety. One side of the FMN isoalloxazine ring faces toward the C-terminal end of the barrel, and the other side is veiled in three long β2−α2, β4−αA (residues 128−138) and β6−α6 loops. In particular, the β4−αA loop, which includes an amino acid sequence that is highly conserved among all DHODs (Figure 1) and has been identified as the active site loop in *L. lactis* DHODA (*22*, *28*) and *E. coli* DHOD (*44*), is located just over the FMN cofactor, preventing an outside solvent from contacting the isoalloxazine ring (Figure 2A). Figure 3 shows amino acid residues and bound water molecules in the FMN cofactor region. Nitrogen and oxygen atoms of the isoalloxazine ring interact via hydrogen bonds with Ala19 O, Lys43 N_ζ, Ser44 O, Asn127 $N_{\delta2}$, Lys164 N_ζ and water D, but the hydrophobic dimethyl benzene moiety lacks close contacts with amino acid residues of TcDHOD. In addition, ribityl hydroxyl groups interact with Ala19 O, Lys164 N_ζ, Val193 O, Cys248 S_γ and water C, and the phosphate group interacts with main chain imino nitrogen atoms of Gly222, Gly250, Gly271 and Thr272 as well as Thr272 $O_{\gamma1}$, water A and B. Three hydrogen bonds formed between Lys164 and the isoalloxazine should play a crucial role in binding FMN to TcDHOD, as indicated by the K164A mutant of *L. lactis* DHODA, to which FMN does not bind (*22*). The negative charge on the phosphate group seems to be stabilized by hydrogen bonds with these main chain imino nitrogen atoms, as has been observed for the oxyanion holes of serine proteases (*45*). There are four water molecules (F, G, H and I) in each cavity formed between the isoalloxazine ring and the β4−αA loop. These water molecules interact with one another and with Asn67 $N_{\delta2}$, Leu71 N, Asn127 $N_{\delta2}$, Asn194 $O_{\delta1}$ and Ser195 O_γ. Most of the amino acid residues referred to here have been completely or well conserved in all known DHOD sequences and participate in interactions with FMN cofactors in the structures of DHODs listed in Figure 1.

Binding of Dihydroorotate, Orotate and Oxonate to TcDHOD. (*S*)-Dihydroorotate, orotate and oxonate are a substrate, product and competitive inhibitor of DHODs, respectively (*21*). Figures 4A−C show that each of these compounds binds to the cavity in the same manner, at the position occupied by waters F, G, H and I in the ligand-free structure. Correspondingly, O8, O4, N3 and O2 of each compound are positionally related to waters F, G, H and I, respectively. In the bound form, orotate and oxonate are in a planar conformation with the exception of their carboxyl oxygen atoms. For dihydroorotate, by contrast, C5 and C6 deviate from the plane constituted by N1, C2, N3, C4, O2 and O4 at a distance and direction of 0.20 Å away from or 0.29 Å toward the isoalloxazine ring, respectively. The dihydroorotate carboxyl group is in an equatorial conformation and faces away from the isoalloxazine ring, whereas the calculated position of the axial C6 hydrogen, H6, is located between C6 and FMN N5 (Figure 4A).

The bound dihydroorotate, orotate and oxonate stack parallel to the isoalloxazine ring and do not appear to cause any discernible changes in the conformation of the TcDHOD polypeptide as compared with the ligand-free form. These compounds interact via hydrogen bonds with Lys43 N_ζ, Asn67 $O_{\delta1}$ and $N_{\delta2}$, Gly70 N, Asn127 $N_{\delta2}$, Asn132 $N_{\delta2}$, Asn194 $O_{\delta1}$ and $N_{\delta2}$, Met69 N, Leu71 N and Ser195 O_γ. The carboxyl groups of dihydroorotate, orotate and oxonate are twisted about their C_6-C_7 bonds with $C_5-C_6-C_7-O_9$ dihedral angles of 98.5°, 127.0° and 113.2°, respectively. Their carboxyl O_8 atoms interact with Lys43 N_ζ and Leu71 N, and their carboxyl O_9 atoms with Gly70 N, Met69 N and Asn132 $N_{\delta2}$ (Figures 4A−C). Interactions that involve protein nitrogen atoms are commonly found in the structures of other DHOD−orotate complexes, and seem to be involved in stabilization of negative charges on their carboxyl groups and of the twisted conformation.

Cys130 in the β4-αA loop, which has previously been identified as the catalytic base in *L. lactis* DHODA (*21*−*23*, *28*, *29*), is located with its S_γ at distances of 3.52 Å, 4.94 Å and 4.46 Å from dihydroorotate C_5, O_8 and O_9, respectively. Nearly equal distances were also determined for the distance between S_γ and orotate C_5, O_8 and O_9 (that is, 3.62 Å, 4.92 Å and 4.66 Å, respectively). In both cases, the distance from S_γ to O_8 or O_9 is too far for the thiol group to interact with either, according to the van der Waals radii for SH (2.34 Å) and O (1.40 Å) (*46*). However, the distances between S_γ and C_5 are favorable for a $S_\gamma\cdots H-C_5$ interaction in the bound dihydroorotate, and for a $S_\gamma-H\cdots C_5$ interaction in the bound orotate (Figures 4A,B).

Oxonate, a competitive inhibitor for all DHODs (*21*) (IC_{50} = 35 μM for TcDHOD), appears to be bound to TcDHOD in the same manner observed for dihydroorotate and orotate

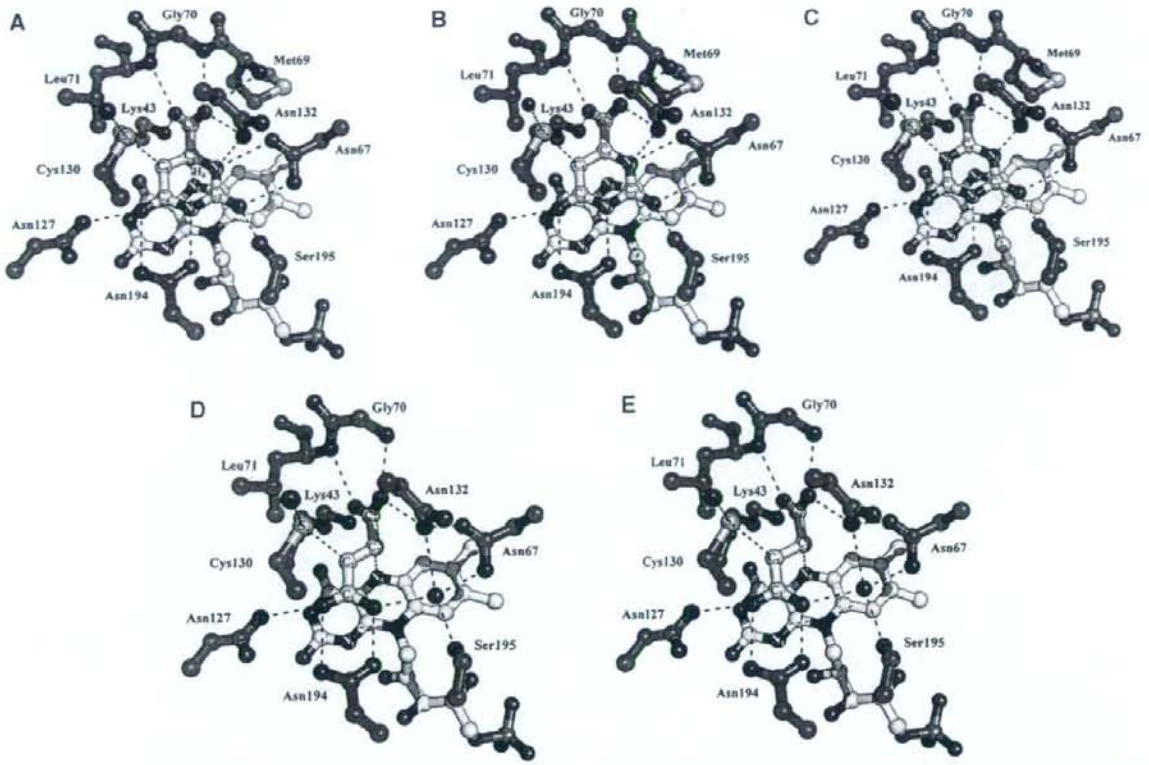

FIGURE 4: Binding of (A) dihydroorotate, (B) orotate, (C) oxonate, (D) fumarate and (E) succinate to TcDHOD. Amino acid residues, FMN and bound compounds are shown as green, yellow or white ball-and-stick models, respectively. The substrates and products of the first half-reaction (dihydroorotate and orotate) and second half-reaction (fumarate and succinate) and a competitive inhibitor (oxonate) are bound to TcDHOD in a similar manner. In (A)−(E), Cys130 Sγ forms a hydrogen bond with water K and is located 3.52 Å, 3.62 Å, 3.42 Å, 3.43 Å and 3.60 Å from dihydroorotate C_5, orotate C_5, oxonate N_5, fumarate C_2 and succinate C_2, respectively. The FMN N_5 is located 3.25 Å, 3.65 Å, 3.66 Å, 3.51 Å and 3.32 Å from dihydroorotate C_6, orotate C_6, oxonate C_6, fumarate C_3 and succinate C_3, respectively. In each structure, possible hydrogen bond interactions are shown only for those between the compounds and TcDHOD, and are represented by dotted lines. The images were generated with PyMOL (http://pymol.sourceforge.net).

(Figure 4C). The distances between oxonate O_9 and Met69 N, oxonate N_1 and Asn67 $O_{\delta 2}$ are longer by 0.28−0.46 Å than those observed in the bound dihydroorotate and orotate. However, an additional hydrogen bond with a distance of 3.41 Å is formed between oxonate N_5 and Cys130 S_γ. This interaction probably contributes to a decrease in the average *B*-factor of the main-chain atoms of the $\beta 4-\alpha A$ loop to 6.9 Å^2 as compared with 9.4 Å^2 and 15.0 Å^2 for the TcDHOD−dihydroorotate and −orotate complexes, respectively, and thus, to suppression of the flexibility of the $\beta 4-\alpha A$ loop.

Binding of Fumarate and Succinate to TcDHOD. Both fumarate and succinate are bound to the same site as dihydroorotate, orotate and oxonate via identical hydrogen bonds with TcDHOD amino acid residues (Figures 4D,E). The bound fumarate and succinate are in a planar conformation, approximately parallel to the isoalloxazine ring, with the exception of the second carboxyl O_3 and O_4 atoms. As observed in the bound dihydroorotate, orotate and oxonate, the second carboxyl groups are twisted about the C3−C4 bonds with $C_2-C_3-C_4-O_4$ dihedral angles of 99.1° and 92.4°, respectively, and interact with protein nitrogen atoms. On the other hand, the first carboxyl C_1, O_1 and O_2 atoms occupy the C_4, O_4 and N_3 positions, respectively, of the bound dihydroorotate *etc.*

C_2 and C_3 of the bound fumarate and succinate are in close contact with Cys130 S_γ and FMN N_5, respectively. The distances between S_γ and C_2 are 3.43 and 3.60 Å for the bound fumarate and succinate, respectively, and those between N_5 and C_3, 3.51 and 3.32 Å. Accordingly, S_γ and C_2, as observed in the bound dihydroorotate *etc.*, are also at a distance favorable for a $S_\gamma-H\cdots C_2$ interaction in the bound fumarate, and for a $S_\gamma\cdots H-C_2$ interaction in the bound succinate (Figures 4D,E).

DISCUSSION

In this study, we determined, at atomic resolution, the structures of TcDHOD in the ligand-free form and in complexes with physiological substrates (dihydroorotate and fumarate) and reaction products (orotate and succinate), as well as in a complex with the competitive inhibitor oxonate. We found that the substrates and products of the first and the second half-reactions bind to the same site of TcDHOD, which is consistent with the one-site ping-pong Bi-Bi mechanism demonstrated by kinetic studies for family 1A DHODs (*14, 26, 27, 47*). The structures of each of the five complexes can be superimposed on the ligand-free structure with an rms deviation in the range 0.11 Å to 0.13 Å for subunit 312 C_α positions, and 0.12 Å to 0.16 Å for dimer

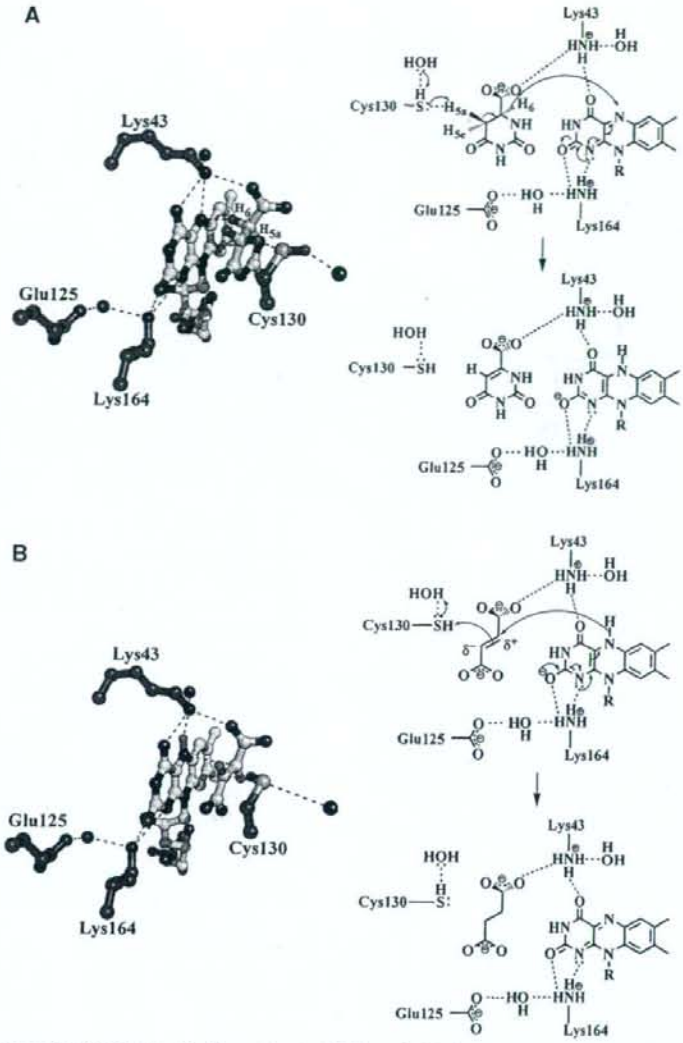

FIGURE 5: Proposed mechanisms for (A) the first half-reaction (oxidation of dihydroorotate to orotate) and (B) the second half-reaction (reduction of fumarate to succinate) as carried out by TcDHOD. The FMN cofactor (yellow), amino acid residues (green) and substrates (white) are represented using ball-and-stick models drawn with PyMOL. The hydrogen atoms of dihydroorotate C5, C6 and Cys130Sγ are shown at their calculated positions (cyan balls).

624 C_α positions. Furthermore, in each structure we determined, both the oxidized and the reduced FMN cofactors are essentially planar, and the FMN cofactor and its peripheral 72 amino acid residues within 8 Å can be superimposed on the ligand-free form, with an rms deviation of 0.06 Å to 0.10 Å between subunits, and 0.08 Å to 0.11 Å between dimers. Thus, the protein and FMN cofactor portions of the complexes are essentially identical with the ligand-free TcDHOD. Although structures determined in this study do not reveal physiological states in the sense that orotate and fumarate bind to TcDHOD with the oxidized FMN cofactor and dihydroorotate binds to TcDHOD with reduced FMN, they should be good models for the TcDHOD enzymatic reaction pathway. On the basis of the X-ray crystal structures determined in this study, here we discuss the mechanisms of the first and the second half-reactions brought about by TcDHOD.

Structural Insight into the First Half-Reaction, Dihydroorotate Oxidation. The mechanism of the first half-reaction has been extensively discussed based on kinetic analyses (*21*, *23*, *24*, *26*, *47*) and crystal structures (*17*, *18*, *28*, *29*), and Cys130 has been identified as the active site base for *L. lactis* DHODA that abstracts a proton from dihydroorotate C_5. In the crystal structure of the TcDHOD−dihydroorotate complex, Cys130 S_γ is 3.52 Å and 3.59 Å away from dihydroorotate C_5 and water K, respectively (Figure 5A). In addition, the calculated positions of the axial C_5 hydrogen, H_{5a}, and Cys130 S_γ hydrogen, H_S, are favorably disposed for the $H_2O^K\cdots H_S-S_\gamma\cdots H_{5a}-C_5$ interaction, as indicated by the distances $S_\gamma-H_{5a}$ (2.54 Å) and $H_S-O^KH_2$ (2.32 Å), and by the angles $S_\gamma-H_{5a}-C_5$ (157.5°) and $S_\gamma-H_S-O^KH_2$ (148.8°). The water K is linked to outside solvents through a hydrogen bond chain formed by three water molecules that are located in a hydrophilic channel connecting Cys130Sγ

to the outside. This channel is also found in family 1A DHODs (2B4G and 2DOR), but it is not found in the K213E mutant of *L. lactis* DHODA (1JQV), in which the active site loop closes the channel. Family 1B DHOD from *L. lactis* (1EP2) does not have this hydrophilic channel; instead, the active site Cys135 is on the molecular surface. Because of this exquisite disposition of Cys130 and the hydrogen bond chain, dihydroorotate H_{5a} would be abstracted by Cys130 as a proton and then relayed to an outside solvent through the hydrogen bond chain.

Together with the proton abstraction from C_5, dihydroorotate H_6 is transferred to FMN N_5 as a hydride (or a hydride equivalent) to reduce the cofactor. As mentioned above in the Results section, the calculated position of H_6 (between C_6 and FMN N_5, 2.19 Å away from FMN N_5, with a $C_6-H_5-N_5$ angle of 160°) is suitably disposed for the hydride transfer. The structure of the TcDHOD−dihydroorotate complex shows that the reduced FMN cofactor is essentially planar, which indicates that it is not neutral reduced FMN, $FMNH_2$, but anionic reduced FMN, $FMNH^-$ (*48*). The negative charge of the anionic reduced FMN is stabilized by Lys43 and Lys164 (Figure 5A). Lys164 is part of the hydrogen bond network of Glu125···H_2O^J···Lys164··· FMN. Although both Glu125 and Lys164 are shielded from outside solvents, a proton would be shifted from the Glu125 carboxyl group to the Lys164 amino group through the hydrogen bond network. Both of the residues are conserved only in the amino acid sequences of DHODs from families 1A and 1B (Figure 1), but inspections of the crystal structures of family 2 DHODs show that alternative glutamate and lysine residues conserved in amino acid sequences of family 2 DHODs (for example, *H. sapiens* DHOD Glu116 and Lys255) similarly form the hydrogen bond network of Glu116···H_2O···Lys255···FMN.

In summary, the first half-reaction proceeds as follows (Figure 5A). After binding of dihydroorotate to TcDHOD, a hydride (or a hydride equivalent) is transferred from dihydroorotate C_6 to FMN N_5, and Cys130 S_γ completes oxidation of dihydroorotate by abstracting a proton from C_5, which is relayed to an outside solvent via the H_2O^K ···H_S-S_γ···$H_{5a}-C_5$ network. The negative charge of the anionic reduced FMN is stabilized by Lys43 and Lys164. This mechanism is consistent with previous works (*18, 23*−*26, 28*−*30*). Although we cannot be sure whether the scission of C_6-H_6 and C_5-H_{5a} bonds is concerted or stepwise, and we cannot be sure whether H_6 is transferred to FMN N_5 as a hydride or a hydride equivalent, the concerted mechanism with the transfer of a hydride equivalent has been proposed for family 1 DHODs (*23*).

Structural Insight into the Second Half-Reaction, Fumarate Reduction. Unlike the physiological substrate of the first half-reaction, those of the second half-reaction differ among the DHOD subfamilies. The reduced FMN cofactor for TcDHOD converts fumarate to succinate, whereas NAD^+ is reduced to NADH by family 1B DHODs, and ubiquinone is reduced to ubiquinol by family 2 DHODs.

The prominent feature we found in the TcDHOD−fumarate complex is that the conformation of the bound fumarate is nonplanar. The second carboxyl group is twisted around the C_3-C_4 bond with a $C_2-C_3-C_4-O_4$ dihedral angle of 99.1° as observed in the bound succinate, dihydroorotate, orotate and oxonate structures. The bound fumarate is twisted by interactions with Lys43 N_ζ, Leu71 N, Gly70 N, and Asn132 $N_{\delta 2}$ (Figure 4D). Twisting around the C_3-C_4 bond breaks the uniform distribution of π-electrons over the conjugated double bonds of fumarate, and partial charge separation, represented as $C_2^{\delta-}$ and $C_3^{\delta+}$, is then induced. Together with the shorter distances of $C_2^{\delta-}$−Cys130 Sδ (3.43 Å) and $C_3^{\delta+}$−FMN N_5 (3.15 Å) than those of $C_3^{\delta+}$− Cys130 Sδ (4.24 Å) and $C_2^{\delta-}$− FMN N_5 (4.03 Å), this partial charge separation may act as a guide, leading a hydride (or hydride equivalent) from FMN N_5 to $C_3^{\delta+}$ and a proton from Cys130 S_γ to $C_2^{\delta-}$ in the thermodynamically favorable reduction of fumarate with reduced FMN. In the same manner as the TcDHOD−dihydroorotate complex, the water K (Figure 5B) was also in the $2F_o - F_c$ electron density map of the TcDHOD−fumarate complex (Supporting Information Figure S2J), and acts a part of the hydrogen bond network $HO^K-H\cdots S_\gamma-H_s\cdots C_2^{\delta-}$. Therefore, a proton can be relayed from an outside solvent to $C_2^{\delta-}$ through the network (Figure 5B).

To find out whether this fumarate twisting is common, we searched the Protein Data Bank for protein structures with fumarate. Ten structures were found. Four [1D4E (*49*), 1P2E (*50*), 2BS2 (*51*), and 1QLB (*52*)] are flavoproteins with fumarate reductase activity, and six [1PJ2 (*53*), 1QCO (*54*), 2CGO (*55*), 2EEO (not published), 2PTQ (*56*), and 2VD6 (not published)] are enzymes in which fumarate is a product (1QCO, 2PTQ, 2VD6), an inhibitor (2CGO, 2EEO), or an allosteric activator (1PJ2). Twisted fumarate is near the isoalloxazine in all fumarate reductases except 2BS2, while a planar fumarate is bound to the other six. Unlike TcDHOD, the distances between $C_2^{\delta-}$ and N_5 (3.38 to 3.96 Å) are comparable with those between $C_3^{\delta+}$ and N_5 (3.35 to 3.89 Å) in 1D4E, 1P2E and 1QLB. Both 2BS2 and 1QLB are quinol:fumarate oxidoreductase from *Wolinella succinogenes*, but 2BS2, in which the active site loop is half-open, is probably unreactive. While the number of examples is small, we speculate that the twisting of fumarate is common in flavoproteins with fumarate reductase activity.

In summary, at atomic resolution we determined the three-dimensional structures of TcDHOD in ligand-free form and in complexes with dihydroorotate, orotate, oxonate, fumarate, and succinate. All structures are essentially identical and include a planar FMN cofactor. The planar reduced FMN cofactor of TcDHOD−dihydroorotate complex indicates that the cofactor is in the form of the anionic reduced FMN. Taking these structures as models of the enzymatic pathway gives insight regarding the catalytic mechanisms of dihydroorotate oxidation and fumarate reduction. We expect that information about the structure of TcDHOD obtained in this study, particularly about interactions between the enzyme and the inhibitor and physiological substrates, will be useful in the design specific and effective inhibitors against TcDHOD.

ACKNOWLEDGMENT

We thank all staff members at beamlines BL44XU at SPring-8 and NW12 at Photon Factory for their help with X-ray diffraction data collection and T. Nakazawa (Nara Women's University) for helpful discussions.

SUPPORTING INFORMATION AVAILABLE

One purification table of recombinant TcDHOD (Table S1), a figure (S1) explaining the pyrimidine *de novo* biosynthesis as well as fumarate and succinate metabolism in *T. cruzi* and a figure (S2) showing detailed electron density map of all ligands complexed with TcDHOD. This material is available free of charge via the Internet at http://pubs.acs.org.

REFERENCES

1. Jensen, K. F., and Bjornberg, O. (1998) Evolutionary and functional families of dihydroorotate dehydrogenases. *Paths Pyrimidines 6*, 20–28.
2. Baldwin, J., Farajallah, A. M., Malmquist, N. A., Rathod, P. K., and Phillips, M. A. (2002) Malarial dihydroorotate dehydrogenase. Substrate and inhibitor specificity. *J. Biol. Chem. 277*, 41827–41834.
3. Gero, A. M., and O'Sullivan, W. J. (1985) Human spleen dihydroorotate dehydrogenase: properties and partial purification. *Biochem. Med. 34*, 70–82.
4. Norager, S., Jensen, K. F., Bjornberg, O., and Larsen, S. (2002) *E. coli* dihydroorotate dehydrogenase reveals structural and functional distinctions between different classes of dihydroorotate dehydrogenases. *Structure 10*, 1211–1223.
5. Liu, S., Neidhardt, E. A., Grossman, T. H., Ocain, T., and Clardy, J. (2000) Structures of human dihydroorotate dehydrogenase in complex with antiproliferative agents. *Structure 8*, 25–33.
6. Marcinkeviciene, J., Rogers, M. J., Kopcho, L., Jiang, W., Wang, K., Murphy, D. J., Lippy, J., Link, S., Chung, T. D., Hobbs, F., Haque, T., Trainor, G. L., Slee, A., Stern, A. M., and Copeland, R. A. (2000) Selective inhibition of bacterial dihydroorotate dehydrogenases by thiadiazolidinediones. *Biochem. Pharmacol. 60*, 339–342.
7. Copeland, R. A., Marcinkeviciene, J., Haque, T. S., Kopcho, L. M., Jiang, W., Wang, K., Ecret, L. D., Sizemore, C., Amsler, K. A., Foster, L., Tadesse, S., Combs, A. P., Stern, A. M., Trainor, G. L., Slee, A., Rogers, M. J., and Hobbs, F. (2000) *Helicobacter pylori*-selective antibacterials based on inhibition of pyrimidine biosynthesis. *J. Biol. Chem. 275*, 33373–33378.
8. Baldwin, J., Michnoff, C. H., Malmquist, N. A., White, J., Roth, M. G., Rathod, P. K., and Phillips, M. A. (2005) High-throughput screening for potent and selective inhibitors of *Plasmodium falciparum* dihydroorotate dehydrogenase. *J. Biol. Chem. 280*, 21847–21853.
9. Heikkila, T., Ramsey, C., Davies, M., Galtier, C., Stead, A. M., Johnson, A. P., Fishwick, C. W., Boa, A. N., and McConkey, G. A. (2007) Design and synthesis of potent inhibitors of the malaria parasite dihydroorotate dehydrogenase. *J. Med. Chem. 50*, 186–191.
10. Palfey, B. A., Bjornberg, O., and Jensen, K. F. (2001) Specific inhibition of a family 1A dihydroorotate dehydrogenase by benzoate pyrimidine analogues. *J. Med. Chem. 44*, 2861–2864.
11. Wolfe, A. E., Thymark, M., Gattis, S. G., Fagan, R. L., Hu, Y. C., Johansson, E., Arent, S., Larsen, S., and Palfey, B. A. (2007) Interaction of benzoate pyrimidine analogues with class 1A dihydroorotate dehydrogenase from *Lactococcus lactis*. *Biochemistry 46*, 5741–5753.
12. Gao, G., Nara, T., Nakajima-Shimada, J., and Aoki, T. (1999) Novel organization and sequences of five genes encoding all six enzymes for de novo pyrimidine biosynthesis in *Trypanosoma cruzi*. *J. Mol. Biol. 285*, 149–161.
13. Nara, T., Hshimoto, T., and Aoki, T. (2000) Evolutionary implications of the mosaic pyrimidine-biosynthetic pathway in eukaryotes. *Gene 257*, 209–222.
14. Takashima, E., Inaoka, D. K., Osanai, A., Nara, T., Odaka, M., Aoki, T., Inaka, K., Harada, S., and Kita, K. (2002) Characterization of the dihydroorotate dehydrogenase as a soluble fumarate reductase in *Trypanosoma cruzi*. *Mol. Biochem. Parasitol. 122*, 189–200.
15. Annoura, T., Nara, T., Makiuchi, T., Hashimoto, T., and Aoki, T. (2005) The origin of dihydroorotate dehydrogenase genes of kinetoplastids, with special reference to their biological significance and adaptation to anaerobic, parasitic conditions. *J. Mol. Evol. 60*, 113–127.
16. Arakaki, T. L., Buckner, F. S., Gillespie, J. R., Malmquist, N. A., Phillips, M. A., Kalyuzhniy, O., Luft, J. R., Detitta, G. T., Verlinde, C. L., Van Voorhis, W. C., Hol, W. G., and Merritt, E. A. (2008) Characterization of *Trypanosoma brucei* dihydroorotate dehydrogenase as a possible drug target; structural, kinetic and RNAi studies. *Mol. Microbiol. 68*, 37–50.
17. Rowland, P., Nielsen, F. S., Jensen, K. F., and Larsen, S. (1997) The crystal structure of the flavin containing enzyme dihydroorotate dehydrogenase A from *Lactococcus lactis*. *Structure 5*, 239–252.
18. Rowland, P., Norager, S., Jensen, K. F., and Larsen, S. (2000) Structure of dihydroorotate dehydrogenase B: electron transfer between two flavin groups bridged by an iron-sulphur cluster. *Structure 8*, 1227–1238.
19. Hurt, D. E., Widom, J., and Clardy, J. (2006) Structure of *Plasmodium falciparum* dihydroorotate dehydrogenase with a bound inhibitor. *Acta Crystallogr., Sect. D: Biol. Crystallogr. 62*, 312–323.
20. Hansen, M., Le Nours, J., Johansson, E., Antal, T., Ullrich, A., Loffler, M., and Larsen, S. (2004) Inhibitor binding in a class 2 dihydroorotate dehydrogenase causes variations in the membrane-associated N-terminal domain. *Protein Sci. 13*, 1031–1042.
21. Bjornberg, O., Jordan, D. B., Palfey, B. A., and Jensen, K. F. (2001) Dihydrooxonate is a substrate of dihydroorotate dehydrogenase (DHOD) providing evidence for involvement of cysteine and serine residues in base catalysis. *Arch. Biochem. Biophys. 391*, 286–294.
22. Bjornberg, O., Rowland, P., Larsen, S., and Jensen, K. F. (1997) Active site of dihydroorotate dehydrogenase A from *Lactococcus lactis* investigated by chemical modification and mutagenesis. *Biochemistry 36*, 16197–16205.
23. Fagan, R. L., Jensen, K. F., Bjornberg, O., and Palfey, B. A. (2007) Mechanism of flavin reduction in the class 1A dihydroorotate dehydrogenase from *Lactococcus lactis*. *Biochemistry 46*, 4028–4036.
24. Fagan, R. L., Nelson, M. N., Pagano, P. M., and Palfey, B. A. (2006) Mechanism of flavin reduction in class 2 dihydroorotate dehydrogenases. *Biochemistry 45*, 14926–14932.
25. Jiang, W., Locke, G., Harpel, M. R., Copeland, R. A., and Marcinkeviciene, J. (2000) Role of lys100 in human dihydroorotate dehydrogenase: mutagenesis studies and chemical rescue by external amines. *Biochemistry 39*, 7990–7997.
26. Jordan, D. B., Bisaha, J. J., and Picollelli, M. A. (2000) Catalytic properties of dihydroorotate dehydrogenase from *Saccharomyces cerevisiae*: studies on pH, alternate substrates, and inhibitors. *Arch. Biochem. Biophys. 378*, 84–92.
27. Marcinkeviciene, J., Jiang, W., Locke, G., Kopcho, L. M., Rogers, M. J., and Copeland, R. A. (2000) A second dihydroorotate dehydrogenase (Type A) of the human pathogen *Enterococcus faecalis*: expression, purification, and steady-state kinetic mechanism. *Arch. Biochem. Biophys. 377*, 178–186.
28. Norager, S., Arent, S., Bjornberg, O., Ottosen, M., Lo Leggio, L., Jensen, K. F., and Larsen, S. (2003) *Lactococcus lactis* dihydroorotate dehydrogenase A mutants reveal important facets of the enzymatic function. *J. Biol. Chem. 278*, 28812–28822.
29. Rowland, P., Bjornberg, O., Nielsen, F. S., Jensen, K. F., and Larsen, S. (1998) The crystal structure of *Lactococcus lactis* dihydroorotate dehydrogenase A complexed with the enzyme reaction product throws light on its enzymatic function. *Protein Sci. 7*, 1269–1279.
30. Mohsen, A. W., Rigby, S. E., Jensen, K. F., Munro, A. W., and Scrutton, N. S. (2004) Thermodynamic basis of electron transfer in dihydroorotate dehydrogenase B from *Lactococcus lactis*: analysis by potentiometry, EPR spectroscopy, and ENDOR spectroscopy. *Biochemistry 43*, 6498–6510.
31. Inaoka, D. K., Takashima, E., Osanai, A., Shimizu, H., Nara, T., Aoki, T., Harada, S., and Kita, K. (2005) Expression, purification and crystallization of *Trypanosoma cruzi* dihydroorotate dehydrogenase complexed with orotate. *Acta Crystallogr., Sect. F: Struct. Biol. Cryst. Commun. 61*, 875–878.
32. Hartree, E. F. (1972) Determination of protein: a modification of the Lowry method that gives a linear photometric response. *Anal. Biochem. 48*, 422–427.
33. Otwinowski, Z., and Minor, W. (1997) Processing of X-ray diffraction data collected in oscillation mode. *Methods Enzymol. 276*, 307–326.
34. Vagin, A., and Teplyakov, A. (1997) MOLREP: an automated program for molecular replacement. *J. Appl. Crystallogr. 30*, 1022–1025.
35. Sariego, I., Annoura, T., Nara, T., Hashimoto, M., Tsubouchi, A., Iizumi, K., Makiuchi, T., Murata, E., Kita, K., and Aoki, T. (2006) Genetic diversity and kinetic properties of *Trypanosoma cruzi* dihydroorotate dehydrogenase isoforms. *Parasitol. Int. 55*, 11–16.

36. Guex, N., and Peitsch, M. C. (1997) SWISS-MODEL and the Swiss-PdbViewer: an environment for comparative protein modeling. *Electrophoresis 18*, 2714–2723.
37. Brunger, A. T., Adams, P. D., Clore, G. M., DeLano, W. L., Gros, P., Grosse-Kunstleve, R. W., Jiang, J. S., Kuszewski, J., Nilges, M., Pannu, N. S., Read, R. J., Rice, L. M., Simonson, T., and Warren, G. L. (1998) Crystallography & NMR system: A new software suite for macromolecular structure determination. *Acta Crystallogr., Sect. D: Biol. Crystallogr. 54*, 905–921.
38. Emsley, P., and Cowtan, K. (2004) Coot: model-building tools for molecular graphics. *Acta Crystallogr. Sect. D: Biol. Crystallogr. 60*, 2126–2132.
39. Murshudov, G. N., Vagin, A. A., and Dodson, E. J. (1997) Refinement of macromolecular structures by the maximum-likelihood method. *Acta Crystallogr., Sect. D: Biol. Crystallogr. 53*, 240–255.
40. Ramachandran, G. N., and Sasisekharan, V. (1968) Conformation of polypeptides and proteins. *Adv. Protein Chem. 23*, 283–438.
41. Laskowski, R. A., MacArthur, M. W., Moss, D. S., and Thornton, J. M. (1993) PROCHECK: a program to check the stereochemical quality of protein structures. *J. Appl. Crystallogr. 26*, 283–291.
42. Collaborative Computational Project, N. 1994, The CCP4 suite: programs for protein crystallography. *Acta Crystallogr., Sect. D: Biol. Crystallogr.* 760–763.
43. Pinheiro, M. P., Iulek, J., and Cristina Nonato, M. (2008) Crystal structure of *Trypanosoma cruzi* dihydroorotate dehydrogenase from Y strain. *Biochem. Biophys. Res. Commun. 369*, 812–817.
44. Bjornberg, O., Gruner, A. C., Roepstorff, P., and Jensen, K. F. (1999) The activity of *Escherichia coli* dihydroorotate dehydrogenase is dependent on a conserved loop identified by sequence homology, mutagenesis, and limited proteolysis. *Biochemistry 38*, 2899–2908.
45. James, M. N., Sielecki, A. R., Brayer, G. D., Delbaere, L. T., and Bauer, C. A. (1980) Structures of product and inhibitor complexes of *Streptomyces griseus* protease A at 1.8 Å resolution. A model for serine protease catalysis. *J. Mol. Biol. 144*, 43–88.
46. Pauling, L. (1960) *The nature of the chemical bond*, 3rd ed., Cornell Univ. Press, Ithaca, NY.
47. Nielsen, F. S., Rowland, P., Larsen, S., and Jensen, K. F. (1996) Purification and characterization of dihydroorotate dehydrogenase A from *Lactococcus lactis*, crystallization and preliminary X-ray diffraction studies of the enzyme. *Protein Sci. 5*, 852–856.
48. Zheng, Y., and Ornstein, R. L. (1996) A theoretical study of the structures of flavin in different oxidation and protonation states. *J. Am. Chem. Soc. 118*, 9402–9408.
49. Leys, D., Tsapin, A. S., Nealson, K. H., Meyer, T. E., Cusanovich, M. A., and Van Beeumen, J. J. (1999) Structure and mechanism of the flavocytochrome *c* fumarate reductase of *Shewanella putrefaciens* MR-1. *Nat. Struct. Biol. 6*, 1113–1117.
50. Rothery, E. L., Mowat, C. G., Miles, C. S., Walkinshaw, M. D., Reid, G. A., and Chapman, S. K. (2003) Histidine 61: an important heme ligand in the soluble fumarate reductase from *Shewanella frigidimarina*. *Biochemistry 42*, 13160–13169.
51. Madej, M. G., Nasiri, H. R., Hilgendorff, N. S., Schwalbe, H., and Lancaster, C. R. (2006) Evidence for transmembrane proton transfer in a dihaem-containing membrane protein complex. *EMBO J. 25*, 4963–4970.
52. Lancaster, C. R., Kroger, A., Auer, M., and Michel, H. (1999) Structure of fumarate reductase from *Wolinella succinogenes* at 2.2 Å resolution. *Nature 402*, 377–385.
53. Tao, X., Yang, Z., and Tong, L. (2003) Crystal structures of substrate complexes of malic enzyme and insights into the catalytic mechanism. *Structure 11*, 1141–1150.
54. Timm, D. E., Mueller, H. A., Bhanumoorthy, P., Harp, J. M., and Bunick, G. J. (1999) Crystal structure and mechanism of a carbon-carbon bond hydrolase. *Structure 7*, 1023–1033.
55. Hewitson, K. S., Lienard, B. M., McDonough, M. A., Clifton, I. J., Butler, D., Soares, A. S., Oldham, N. J., McNeill, L. A., and Schofield, C. J. (2007) Structural and mechanistic studies on the inhibition of the hypoxia-inducible transcription factor hydroxylases by tricarboxylic acid cycle intermediates. *J. Biol. Chem. 282*, 3293–3301.
56. Tsai, M., Koo, J., Yip, P., Colman, R. F., Segall, M. L., and Howell, P. L. (2007) Substrate and product complexes of *Escherichia coli* adenylosuccinate lyase provide new insights into the enzymatic mechanism. *J. Mol. Biol. 370*, 541–554.

BI800413R

Acta Crystallographica Section F
Structural Biology and Crystallization Communications
ISSN 1744-3091

Screening of detergents for solubilization, purification and crystallization of membrane proteins: a case study on succinate:ubiquinone oxidoreductase from *Escherichia coli*

Hironari Shimizu,[a] Coh-ichi Nihei,[a]‡ Daniel Ken Inaoka,[a] Tatushi Mogi,[a] Kiyoshi Kita[a] and Shigeharu Harada[b]*

[a]Department of Biomedical Chemistry, Graduate School of Medicine, The University of Tokyo, 7-3-1 Hongo, Bunkyo-ku, Tokyo 113-0033, Japan, and [b]Department of Applied Biology, Graduate School of Science and Technology, Kyoto Institute of Technology, Sakyo-ku, Kyoto 606-8585, Japan

‡ Present address: Department of Microbiology, Graduate School of Medicine, The University of Tokyo, 7-3-1 Hongo, Bunkyo-ku, Tokyo 113-0033, Japan.

Correspondence e-mail: harada@kit.ac.jp

Received 19 February 2008
Accepted 18 August 2008

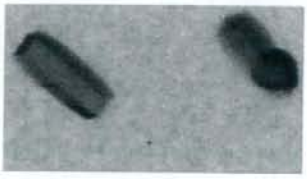

Succinate:ubiquinone oxidoreductase (SQR) was solubilized and purified from *Escherichia coli* inner membranes using several different detergents. The number of phospholipid molecules bound to the SQR molecule varied greatly depending on the detergent combination that was used for the solubilization and purification. Crystallization conditions were screened for SQR that had been solubilized and purified using 2.5%(*w*/*v*) sucrose monolaurate and 0.5%(*w*/*v*) Lubrol PX, respectively, and two different crystal forms were obtained in the presence of detergent mixtures composed of *n*-alkyl-oligoethylene glycol monoether and *n*-alkyl-maltoside. Crystallization took place before detergent phase separation occurred and the type of detergent mixture affected the crystal form.

1. Introduction

Membrane proteins consist of one or more hydrophobic regions that are buried in the membrane as well as hydrophilic regions that contain charged or polar residues that are exposed to water. For crystallization, membrane proteins are usually solubilized from the membranes using a detergent and then purified in the presence of a detergent. The membrane proteins thus prepared are water-soluble protein–detergent complexes in which the membrane-anchored hydrophobic portions are covered with amphiphilic detergent molecules. Crystallization of membrane proteins has been carried out using these protein–detergent complexes. Since the successful crystallization of bacteriorhodopsin (Michel & Oesterheld, 1980) and porin (Garavito & Rosenbusch, 1980) in 1980, many membrane proteins have been crystallized and there are currently 167 unique structures (http://blanco.biomol.uci.edu/Membrane_Proteins_xtal.html) in the Protein Data Bank. However, the crystallization of membrane proteins is still a difficult task and the quality of the crystals obtained has often been insufficient for X-ray diffraction studies. One of the obstacles in the crystallization of membrane proteins is that detergents suitable for solubilization, purification and crystallization must be found by trial and error.

Succinate:ubiquinone oxidoreductase (SQR) is a member of the citric acid cycle and catalyzes the oxidation of succinate to fumarate in conjunction with the reduction of ubiquinone to ubiquinol during aerobic respiration. The enzyme from *Escherichia coli* inner membranes consists of four subunits with five prosthetic groups: one covalently bound FAD, three Fe–S clusters and one haem *b*. The flavoprotein subunit (70 kDa) and Fe–S-containing subunit (30 kDa) are hydrophilic and contain all of the prosthetic groups except for the haem *b*, which is contained in two smaller membrane-anchoring subunits (14 and 13 kDa). As *E. coli* SQR can easily be purified in large quantities according to an established method (Kita *et al.*, 1989) and the X-ray structure has already been determined by Yankovskaya *et al.* (2003) at 2.6 Å resolution, the enzyme appears to be suitable for studies of membrane-protein crystallization. In this work, the phospholipid contents of *E. coli* SQR preparations obtained after solubilization and purification using different detergents were analyzed. Screening of crystallization conditions was performed for

SQR that was prepared using sucrose monolaurate and Lubrol PX for solubilization and purification, respectively, and two new crystal forms were obtained in the presence of detergent mixtures composed of *n*-alkyl-oligoethylene glycol monoether and *n*-alkyl-maltoside.

2. Methods

2.1. Expression and preparation of membranes

A *Bam*HI fragment (*sdhCDAB*) was inserted into pLC339 vector as described by Kita *et al.* (1989). The plasmid was introduced into *E. coli* K12 strain ST4785/pGS133, which lacks the cytochrome *bo* operon. Cells were grown aerobically at 310 K in a 10 l jar fermentor containing LB medium (Miller, 1972) and kanamycin (50 mg l^{-1}) under vigorous agitation and aeration. The addition of kanamycin was essential for the overproduction of *E. coli* SQR, which was at least sixfold higher than in the wild-type strain. The cells were harvested in the late exponential phase of growth and washed in 50 m*M* Tris–HCl buffer pH 7.4 containing 3 m*M* EDTA and 0.1 m*M* PMSF. The typical yield was about 200 g of wet cells from 10 l of culture. Membrane vesicles were prepared from freshly grown cells (200 g) suspended in 500 ml 50 m*M* Tris–HCl buffer pH 7.4 containing 20 m*M* EDTA and a protease-inhibitor cocktail (Sigma) by EDTA/lysozyme treatment followed by disruption with a French press (Yamato *et al.*, 1975). After the removal of any unbroken cells by low-speed centrifugation, membranes were pelleted by ultracentrifugation at 200 000*g* for 2 h at 277 K. The pellet was suspended in 600 ml buffer solution (50 m*M* Tris–HCl pH 7.4 and 10 m*M* EDTA) and the suspension (25 ml) loaded onto buffer (50 ml) containing 44%(*w*/*v*) sucrose was centrifuged at 200 000*g* for 2 h in a Hitachi P45AT fixed-angle rotor. The reddish-brown coloured band of membranes which formed in the middle of the ultracentrifugation tube was separated from the white pellet. The membrane fraction was diluted four times with the buffer and then precipitated by centrifugation at 200 000*g* for 2 h. The pellet was resuspended in a minimum amount of buffer (~80 ml) containing 10%(*w*/*v*) sucrose.

2.2. Estimation of SQR concentration

Since the absorbances at 280 nm (A_{280}s) of the detergents and chemicals in the buffer solutions used in this study were small, the concentration of the *E. coli* SQR was estimated using the calculated molar extinction coefficient at 280 nm (ε_{280} = 129 440), giving A_{280} = 10.6 for a pure SQR solution at 10 mg ml^{-1}. The ε_{280} value was calculated using $\varepsilon_{280} = 5690n_x + 1280n_y$ (Edelhoch, 1967), where 5690 and 1280 are the molar absorption coefficients at 280 nm of tryptophan and tyrosine and n_x and n_y are the number of tryptophan and tyrosine residues in *E. coli* SQR, respectively.

2.3. Assay for phospholipid content

The phospholipid content was assayed using the Fiske–SubbaRow method (Bartlett, 1959). A suitable quantity of the membrane suspension or purified SQR preparation was mixed with 0.5 ml 10 *N* H_2SO_4 in a clean glass test tube and heated in an oven at 423–433 K for more than 3 h. Organic compounds were dehydrated and decomposed to carbon by the H_2SO_4 and the inorganic phosphorus was liberated from the phospholipid. After the addition of several drops of 30% H_2O_2, the solution was again heated (423–433 K) for at least 1.5 h. 4.6 ml 0.22%(*w*/*v*) ammonium molybdate and 0.2 ml of the Fiske–SubbaRow reagent (Bartlett, 1959) were added to the solution, mixed thoroughly and heated for 7 min in a boiling water bath. The colourless solution turned blue and the absorbance at 830 nm (A_{830}) was measured. The concentration of the phosphorus liberated from the phospholipid was estimated from the A_{830} values of standard solutions containing an inorganic phosphate compound of known concentration. For simplicity, we assumed that the phospholipid contained only one P atom unless described otherwise. The A_{830} given by 0.02 µmol PO_4^{3-} is about 0.2 and thus 1 mg of SQR (0.008 µmol) with one bound phospholipid molecule produces an A_{830} of about 0.08. The concentration of the phospholipid in the membrane suspension prepared as described above was about 20 m*M*.

2.4. Solubilization and purification of SQR

In this study, two new crystal forms of *E. coli* SQR were obtained using a preparation that was solubilized from the membranes using 2.5%(*w*/*v*) sucrose monolaurate (CMC = 0.4 m*M*; Dojindo) and purified in the presence of 0.5%(*w*/*v*) Lubrol PX (Nacalai Tesque). Lubrol PX, which is a cheaper detergent than sucrose monolaurate, is a mixture of C_nH_{2n+1}-$(OCH_2CH_2)_m$-OH (abbreviated as C_nE_m) with different-length hydrocarbon and ethylene glycol chains and is virtually the same detergent as THESIT used by Yankovskaya *et al.* (2003). The membrane suspension prepared from 100 g of *E. coli* cells was diluted with buffer solution (20 m*M* Tris–HCl pH 7.4, 10 m*M* $MgCl_2$ and 2 m*M* sodium malonate) to give a phospholipid concentration of 4 m*M* and a freshly prepared 25%(*w*/*v*) sucrose monolaurate solution (477 m*M*) was stirred into the suspension until a final concentration of 2.5%(*w*/*v*) was achieved. After stirring for 1 h at 277 K, the solution was centrifuged at 200 000*g* for 1 h. The clear reddish-brown supernatant containing the solubilized SQR was applied onto a column of GE Healthcare DEAE Sepharose FF (500 ml bed volume) equilibrated with buffer *A* [20 m*M* Tris–HCl pH 7.4, 2 m*M* sodium malonate and 0.5%(*w*/*v*) Lubrol PX]. After washing the column with 2000 ml buffer *A*, SQR was eluted with 4000 ml of buffer *A* containing a linear gradient of 0.0–0.3 *M* NaCl. Fractions containing SQR (A_{412}/A_{280} > 0.5; Fig. 1, lane 1) were pooled. Solid polyethylene glycol 3350 (PEG 3350) was gradually added (30 g per 100 ml) to the pooled fraction containing about

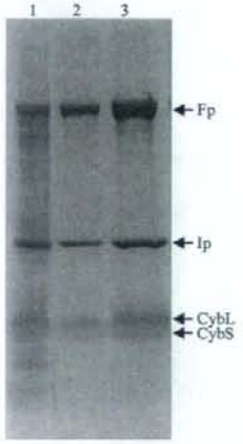

Figure 1
A 12% SDS–PAGE gel stained with Coomassie Brilliant Blue showing the purity of the purified *E. coli* SQR. Lane 1, an eluted fraction from DEAE Sepharose FF; lane 2, an eluted fraction from Source 15Q; lane 3, the purified SQR after sucrose density-gradient ultracentrifugation. Hydrophilic (Fp and Ip) and hydrophobic (CybL and CybS) subunits are shown by arrows.